

A novel carbon electrode for up-scaling flexible perovskite solar cells

Woraprom Passatorntaschakorn^a, Warunee Khampa^a, Wongsathon Musikpan^a, Chawalit Bhoomanee^a, Athipong Ngamjarurojana^a, Sakhorn Rimjaem^{a,b,c}, Atcharawon Gardchareon^{a,c}, Chatchai Rodwihiok^d, Han S. Kim^d, Nutcha Khambunkoed^e, Ratchadaporn Supruangnet^f, Hideki Nakajima^f, Ladda Srathongsian^g, Pongsakorn Kanjanaboops^g, Akarin Intaniwet^h, Anusit Kaewprajakⁱ, Pisist Kumnorkaewⁱ, Fabrice Goubard^j, Pipat Ruankham^{a,b,c,*1}, Duangmanee Wongratanaphisan^{a,b,c,*1}

^a Department of Physics and Materials Science, Faculty of Science, Chiang Mai University, Chiang Mai 50200, Thailand

^b Research Unit for Development and Utilization of Electron Linear Accelerator and Ultrafast Infrared/Terahertz Laser, Chiang Mai University, Chiang Mai 50200, Thailand

^c Thailand Center of Excellence in Physics (ThEP Center), Ministry of Higher Education, Science, Research and Innovation, Bangkok 10400, Thailand

^d Civil and Environmental Engineering, Konkuk University, 120 Neungdong-ro, Gwangjin-gu, Seoul 05029, South Korea

^e College of Electrical and Computer Engineering, National Yang Ming Chiao Tung University, Hsinchu 300093, Taiwan

^f Synchrotron Light Research Institute, Nakhon Ratchasima 30000, Thailand

^g School of Materials Science and Innovation, Faculty of Science, Mahidol University, Nakhon Pathom 73170, Thailand

^h School of Renewable Energy, Maejo University, Chiang Mai 50290, Thailand

ⁱ National Nanotechnology Center (NANOTEC), National Science and Technology Development Agency (NSTDA), 111 Thailand Science Park, Pathum Thani 12120, Thailand

^j CY Cergy Paris Université, LPPI, F-95000 Cergy, France

ARTICLE INFO

Keywords:

Carbon electrode
Carbon quantum dots
Flexible perovskite solar cells
Solvent interlacing
rGO-PEG composites

ABSTRACT

Carbon-based perovskite solar cells (C-PSCs) possess the beneficial attributes of a simple fabrication process, superior stability, and cost-effectiveness. However, flexible C-PSCs have a relatively lower device efficiency when compared to rigid C-PSCs, the reason for which is mainly the poor interface contact between the hole transporting layer (HTL) and the carbon electrode. Herein, a novel carbon electrode (C-rCP) grafted by reduced graphene oxide (rGO)-carbon quantum dots (CQDs)-polyethylene glycol (PEG) composites, is prepared using a modified, room-temperature ethanol solvent interlacing process with a magnetic stirring. Owing to a simple press transfer method used, C-rCP is well suited as counter electrodes of C-PSCs due to their lower sheet resistance; higher density; excellent bendability; suitable thickness; great self-adhesion; and appropriate energy band arrangement that can improve carrier transport, as well as enhance the HTL/carbon interface contact. The best flexible C-PSCs with an area of 0.04 cm² achieve a power conversion efficiency (PCE) of 12.34%. Furthermore, PCEs of 8.80% and 21.61% based flexible C-PSCs with an area of 1.00 cm² are achieved under 1 sun and 1000 lux illuminations, respectively. The introduction of this C-rCP offers an effective method of up-scaling and developing flexible and rigid C-PSCs for future eco-commercialization.

1. Introduction

In recent decades, perovskite solar cells (PSCs) have been the next-generation photovoltaic technologies that having a significant amount of attention. This is due to their excellent semiconductor material qualities, low cost and simple fabrication processes that are comparable

to that of commercial silicon solar cells [1–3]. Owing to these fascinating properties, ongoing work on morphological optimization and surface engineering has seen rapid breakthroughs in single-junction PSC efficiency records. In a short period of time, the power conversion efficiency (PCE) was enhanced from 3.8% (2009) to 25.8% (2021) [4–9]. This excellent technology should be improved further to develop the

* Corresponding authors at: Department of Physics and Materials Science, Faculty of Science, Chiang Mai University, Chiang Mai 50200, Thailand.

E-mail addresses: pipat.r@cmu.ac.th (P. Ruankham), duangmanee.wong@cmu.ac.th (D. Wongratanaphisan).

¹ These authors contributed equally to this work.

technological requirements for large-scale manufacturing, long-term stability, and eco-commercialization of solar cells [10].

The metal halide perovskite film deposition process at low temperatures allows for the development of flexible and lightweight PSC devices based on polymer substrates [11]. Research has continued since the first report published in 2013 on flexible perovskite solar cells (FPSCs) with a PCE of 2.62% [12], and the highest attained PCE on record of 24.7% in 2022 [13]. However, the electrode in PSCs is usually prepared by noble metal that has undergone with high-cost and high-technology requirements. In especially, if this metal is gold (Au) or silver (Ag), it may restrict the production of PSCs on a large-scale [14]. Moreover, the chemical reaction between the perovskite and metal components, gold and silver may cause a rapid decrease in the performance of the cell [15]. This indicates important limitations to establishing great stability in these metal electrode-based devices.

Carbon materials, including carbon black, carbon nanotubes, graphite, and graphene have been suggested as great alternatives. This is due to their abundance and unique properties, which include p-type electrical conductivity, ultra-low cost, outstanding chemical stability, good water resistance, high mechanical strength, appropriate fermi level (~ 5.0 eV), and eco-friendly preparation [16–21]. Furthermore, carbon-based nanomaterials such as reduced graphene oxide (rGO) and carbon quantum dots (CQDs) have been used as passivates in the PSCs to enhance performance and stability, which is owned to their remarkable electrical, optical and chemical properties [22–24]. Amazingly, carbon electrodes can be applied to both rigid and flexible substrates using low-temperature methods. They are a preferred option over metal electrodes and a top choice as an electrode in PSCs [25,26].

Carbon-based perovskite solar cells (C-PSCs) have gained significant attention in recent years due to their simple and low-cost fabrication processes, as well as their excellent long-term stability properties [27–30]. Since the first report on C-PSCs with a mesoporous hole transporting layer (HTL)-free structure by Ku et al. [31], the performance of C-PSCs has improved significantly, achieving a current record PCE of 20.04% in 2022 using a planar C-PSC structure [32]. The highest PCE of planar C-PSCs was achieved by employing carbon paste-based electrodes on top of organic HTL (spiro-OMeTAD [2,2',7,7'-Tetrakis[N, N-di(4-methoxyphenyl)amino]-9,9'-spirobifluorene]) using ethanol solvent exchange and press transfer method. This method has several advantages, such as low temperatures processing, high reproducibility, and cost-effectiveness.

Furthermore, carbon-based flexible PSCs (C-FPSCs) are regarded as “a new era of solar cells” due to their lighter weight, high flexibility, and wider range of applications, making them superior to traditional rigid glass perovskite solar cells. In an initial study, Zhou et al. successfully fabricated planar C-PSCs on both rigid fluorine-doped tin oxide (FTO) glass-based and flexible indium tin oxide (ITO)/poly(ethylene 2,6-naphthalate) (PEN)-based substrates, with active areas of 0.12 cm^2 , achieving the PCEs of 8.73% and 4.29%, respectively [33]. In another study, Deng et al. developed all-room-temperature-processed planar C-PSCs with an active area of 0.09 cm^2 on both rigid and flexible substrates, achieving PCEs of 14.5% and 10.4%, respectively. They employed SnO₂ as the electron transporting layer (ETL) and a cheap hygroscopic polymer, polyethylene glycol (PEG), as the interface passivation layer. This effectively reduced the defect state density of perovskite layer and promoted reliable charge transfer from the perovskite to carbon [34]. For large-area fabrication of planar C-FPSCs, Peng et al. reported a carbon/conductive cloth composites electrode made using the ethanol solvent-exchange process [35]. The use of ethanol molecules in the layer facilitates faster evaporation, resulting in low resistance and high flexibility in heat-press transferred C-FPSCs with carbon/conductive cloth film. The PCEs obtained from this technique were 15.37% and 14.05% for small-area (0.1 cm^2) and large-area (1 cm^2) flexible devices, respectively. These finding represent significant progress in the development of low-cost and simple techniques for the large-scale manufacturing of C-FPSCs.

In our previous report, we successfully enhanced the efficiency and stability of C-PSCs with perovskite film by utilizing carbon paste-based electrodes prepared through a room-temperature ethanol solvent interlacing process for 2 h. This green and simple method helped remove and interlace some of the binders in carbon paste that can negatively affect PSC performance due to the excess binder containing C=O functional group in the carbon films [36]. We then utilized these carbon electrodes to fabricate the C-PSCs with several different ETLs including TiO₂ [37–39], ZnO [40], ZTO [41], TZO [42] and inorganic HTLs such as CuSCN [43]. We also developed them on a 1 cm^2 -area based on C-PSCs on a rigid-FTO substrate [44]. The press transfer was used to transfer the carbon paste electrode to the substrate, further improving the efficiency of the C-PSCs. This process was carried out using a homemade air-filled dry glove box, which is a low-cost and simple alternative to commercial glove boxes. However, the mismatch between the C-FPSCs structure and the carbon electrodes leads to high series resistance and carrier recombination from a lack of the interface contact between the HTL and the carbon electrodes. As a result, reports of large-scale C-FPSCs are rare, and the efficiency of C-FPSCs is lower compared to the most recent metal-based devices [45–47].

Herein, we report a novel carbon electrode for use in C-FPSCs with perovskite films fabricated in a homemade air-filled dry glove box. This carbon electrode, denoted C-rCP, is prepared using a modified room-temperature ethanol solvent interlacing process [36], significantly shortened the processing time with a magnetic stirring. This process involves incorporating rGO and PEG composites along with Thai coffee ground waste-CQDs ethanol based solution. The use of Thai coffee grounds waste in the synthesis of CQDs is not only environmentally friendly, but also a cost-effective approach sine coffee grounds are a widely available waste product. The introduction of rGO-CQDs-PEG (rCP) composites offers a passivated macro-porous gap in carbon paste by solvent engineering to deal with the defects in carbon films and lacking between the HTL/carbon interface issues. This is achieved through the arrangement of rGO in a two-dimensional (2D) layer configuration and the enclosing CQDs within three-dimensional (3D) frameworks. Consequently, self-supporting PEG-composites are formed within the carbon paste. By incorporating these CQDs into carbon films, the resulting C-rCP films exhibit improved conductivity and density, making them a suitable candidate for use as top electrodes in C-FPSCs. The C-rCP films have lower sheet resistance and suitable energy band arrangement, leading to better carrier transport and enhanced HTL/carbon interface. The films also exhibit improved adhesion at the HTL/carbon interface due to their higher density, greater flexibility, suitable thickness and increased self-adhesiveness. Notably, C-rCP devices achieve the highest best and average PCE values in both small- and large-scale areas. Under 1 sun illumination, significant PCEs of 12.34% and 8.80% are achieved by flexible C-rCP devices (18.32% and 12.70% for rigid C-rCP devices) for small-area (0.04 cm^2) and large-area (1.00 cm^2), respectively. Additionally, these large-area devices offer potential for indoor applications, with remarkable PCEs of 27.70% and 21.61% for rigid and flexible substrates, respectively, under LED light 1000 lux illumination. Moreover, the long-term stability of all C-rCP devices is exceptional with an average of over 80% of their initial PCE retained after 1000 h of storage under ambient air environment without encapsulation. Furthermore, the flexible C-rCP devices exhibit excellent mechanical durability, maintaining an average of 80% of the initial PCE after 1200 bending cycles. These results suggest that the C-rCP electrode is a promising way to enhance the performance and stability of flexible devices.

2. Experimental

2.1. Preparation of rCP-Ethanol solution

Firstly, reduced graphene oxide (rGO, for short named *r*) powder (Graphene Deep Tech (Thailand) Co., Ltd.) [48] and polyethylene glycol

(PEG, for short named P) (M_n 20,000, Sigma-Aldrich, USA) [49] were mixed with a ratio of 1:1 (w/w) in ethanol solution (70% v/v) at a concentration of 1 mg ml^{-1} by ultrasonication for 2 h. Then, the *r*GO-PEG dispersions were centrifuged (4,000 rpm, 10 min and 25°C). After that the *r*GO-PEG solution was mixed in coffee-carbon quantum dots (CQDs, for short named C) based ethanol solution (0.5 mg ml^{-1}). The coffee-CQDs were synthesized as follow: 40 mg of Thai arabica 100% coffee ground waste (CMU coffee, Thailand) was dissolve in 20 ml of ethanol solution in Teflon-lined autoclaving tube, and subjected to a hydrothermal technique at 160°C for 12 h, followed by cooling to 25°C . After that the obtained solution was filtered using a filter paper (0.45 μm) and dialyzed with dialysis tubing (3.5 kD, Spectrum Lab. Inc., New Brunswick, NJ, USA) against ethanol solution (25°C for 24 h) [50]. Lastly, the *r*CP-Ethanol solution was sonicated at 25°C for 1 h.

2.2. Preparation of room-temperature carbon films

The carbon films were prepared and modified using the ethanol solvent interlacing process from our previous report [36]. Firstly, the commercial conductive carbon paste (JELCON CH-8, Jujo Chemical Co., Ltd, Japan) was coated on top of the clean glass substrates with a simple doctor-blading method, resulting in wet carbon films. Then, some of the wet carbon films were soaked in the pure ethanol solution (labelled as C) and the remaining ones were soaked in the *r*CP-ethanol based solution (labelled as C-*r*CP). This fast and simple process effectively removed and interlaced residual binders in the carbon paste (**Supplementary Video**) using a Teflon-lined magnetic bar stirred at 400 rpm for 10 min under ambient air conditions ($\sim 25\text{--}30^\circ\text{C}$). Next, both carbon films were peeled off the glass substrates and dried at room-temperature for 30 min. Finally, both carbon films were cut into the area of 0.16 cm^2 for laboratory-scale devices and 1.00 cm^2 for large-scale devices using UV-355 nm laser cutting machine (EZCAD3, China).

2.3. Fabrication of C-PSCs on rigid substrate

The rigid FTO/glass ($15 \Omega \text{ square}^{-1}$, TEC15, Greatcell Solar, Australia) substrates were cleaned with alconox detergent, distilled water, acetone, and 2-propanol under ultrasonic irradiation for 15 min, respectively. After being dried with dry-air gas, the substrates were treated by UV-ozone for 15 min. For the ETL, the low-temperature TiO_2 -NPs solution synthesized with the non-hydrolytic sol-gel process [39, 51–54] was spin-coated on top of the rigid FTO/glass substrates at 1500 rpm for 40 s, followed by annealing at 155°C for 30 min. Then, the TiO_2 -NPs coated substrates were treated with UV-ozone for 10 min. The perovskite ($\text{Cs}_{0.17}\text{FA}_{0.83}\text{Pb}(\text{I}_{0.83}\text{Br}_{0.17})_3$) precursor contained formamidinium iodide (FAI, 99.99%, Greatcell Solar), cesium iodide (CsI, 99.9%, Sigma Aldrich), lead iodide (PbI_2 , 98%, Sigma Aldrich) and lead bromide (PbBr_2 , 98%, Sigma Aldrich) which were dissolved in N, N-dimethylformamide (DMF, anhydrous 99.8%, Sigma Aldrich) and dimethyl sulfoxide (DMSO, anhydrous 99.9%, Sigma Aldrich) with a volume ratio of 4:1. For the perovskite layer, the perovskite precursor was spin-coated at 1000 rpm for 10 s and 4000 rpm for 30 s. Then $180 \mu\text{L}$ of anisole (anhydrous 99.7%, Sigma Aldrich) was dropped onto the spinning substrate during the last 5 s. To form a crystalline perovskite layer, the perovskite films were annealed at 130°C for 15 min under a homemade air-filled dry glove box ($25\text{--}30^\circ\text{C}$, 15–18%RH) [37,38]. For the HTL, the spiro-OMeTAD solution used was prepared by dissolving 72.5 mg of spiro-OMeTAD, $28.7 \mu\text{L}$ of 4-tert-butylpyridine and $17.5 \mu\text{L}$ of lithium bis(trifluoromethanesulfonyl)imide (LiTFSI) solution (520 mg ml^{-1} in acetonitrile) into 1 mL of chlorobenzene (CB, anhydrous 99.8%, Sigma Aldrich). The HTL solution was spin-coated onto the perovskite films at 3000 rpm for 30 s. Finally, the different carbon films with ethanol solvent interlacing were used as the top electrodes and directly pressed on top of the HTL for 10 min at room temperature. Then, they were further heat-pressed at 50°C for 3 min under a constant pressure of 0.6 MPa. For the devices with an active area of 1.00 cm^2 , a graphite

sheet was heat-pressed on top of the carbon layer for 30 s to increase the electrode conductivity [44,46].

2.4. Fabrication of C-FPSCs on flexible substrate

The flexible ITO/PEN ($<15 \Omega \text{ square}^{-1}$, Sigma-Aldrich) substrates were cleaned with 2-propanol under ultrasonic irradiation for 5 min. After being dried with dry-air gas, the substrates were treated by UV-ozone for 5 min. For the ETL, the TiO_2 -NPs solution was spin-coated on top of the ITO/PEN substrates at 4000 rpm for 40 s, followed by annealing at 120°C for 15 min. Then, the TiO_2 -NPs coated substrates were treated with UV-ozone for 5 min. For the perovskite layer, the perovskite precursor was spin-coated at 1000 rpm for 10 s and 5000 rpm for 30 s. Then $180 \mu\text{L}$ of anisole was dropped onto the spinning substrate during the last 5 s. To form a crystalline perovskite layer, the perovskite films were annealed at 100°C for 15 min in an air-filled dry glove box ($25\text{--}30^\circ\text{C}$, 15–18%RH). After that, the HTL solution was spin-coated onto the perovskite films at 4000 rpm for 30 s. Finally, the different carbon films were used as the top electrodes and directly pressed on top of the HTL using similar recipies on rigid substrate, and lowering the temperature of heat-pressing to 30°C for flexible substrate.

3. Results and discussion

In this study, we enhanced the room-temperature ethanol solvent interlacing process [36] by introducing magnetic stirring (as demonstrated in the **Supplementary Video**) to shorten the processing time, as illustrated in **Fig. 1a**. This fast and simple process effectively extracts remove residual binders from the carbon paste and interlaces its constituents. Firstly, the commercial graphite/carbon black conductive carbon paste was coated onto clean glass substrates with the simple doctor-blading method. Subsequently, the as-prepared wet carbon films were separately soaked in two different solutions: *r*GO-CQDs-PEG in ethanol solution (referred to as *r*CP-Ethanol) and pure ethanol solution. Both ethanol-based solutions are capable of extracting some residual binder and interlacing it into the carbon film framework, which could potentially prevent overcuring of the films [55]. After being soaked and dried under ambient air conditions, the carbon films obtained from the *r*CP-Ethanol solution were labeled as C-*r*CP, while the carbon films obtained from the pure ethanol solution were labeled as C. The C-*r*CP films were modified by grafting *r*GO in two-dimensional (2D) layer arrangement and enclosing CQDs in three-dimensional (3D) frameworks, which resulted in the formation of self-supporting PEG-composites. As seen in **Fig. 1b**, the *r*CP-Ethanol and ethanol solutions exhibit different colours when viewed under visible-light and 365 nm UV-light. The *r*CP-Ethanol solution, indicated by the red box, is prepared by mixing the *r*GO-PEG composites solution (left inset) and the coffee-CQDs solution (right inset), and is visibly responsive to ambient exposure to a 365 nm UV light. In addition, the photoluminescence (PL) of the *r*CP-Ethanol solution shows a peak blue emission at 455.1 nm (**Fig. S1, Supplementary material**). The surface morphology and size distribution of coffee-CQDs derived from Thai coffee ground waste were investigated by TEM characterization, as shown in **Fig. S2** of the **Supplementary material**. The coffee-CQDs were found to have a particle size of about 5 nm, with an average lateral dimension (**Fig. S2a, Supplementary material**) and a crystal structure with a lattice spacing of approximately 0.19 nm (**Fig. S2b, Supplementary material**). This lattice spacing corresponds to the [1–111] lattice fringe of graphitic carbon [56]. The particle size analysis using dynamic light scattering (DLS) shows that the *r*CP-Ethanol solution (before soaking the carbon films) has an average size of 216.6 nm (**Fig. S3a, Supplementary material**), corresponding to the HR-TEM image of *r*CP-composites with a size of about 255 nm (**Fig. S3b, Supplementary material**). To investigate the individual role of each of the three components in the *r*CP-Ethanol solution, the carbon films were soaked in different ethanol-based solutions, including pure ethanol (Type I), *r*GO-Ethanol, CQDs-Ethanol, PEG-Ethanol (Type II). In

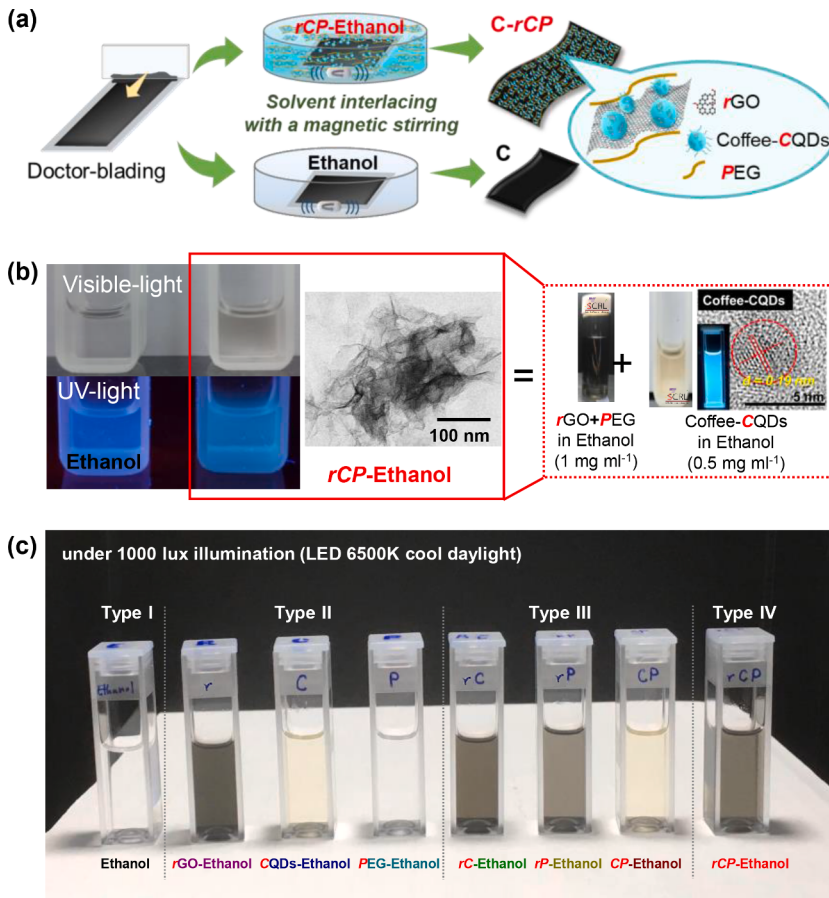


Fig. 1. (a) Schematic diagram of the room-temperature carbon films preparation using a modified ethanol solvent interlacing process with a magnetic stirrer. The two types of carbon films prepared are labeled as C-rCP (top) and C (bottom). (b) PL response of different ethanol-based solutions under an excitation wavelength of 365 nm (top: under visible light, bottom: under UV-light). The red box in the diagram on the right represents the rCP-Ethanol solution created by mixing solutions of rGO-PEG (left inset) and coffee-CQDs (right inset). (c) Photographs of the freshly prepared ethanol-based solutions used for soaking the carbon films. Each solution is categorized based on its components, which include pure ethanol (Type I), one component solution such as rGO-Ethanol, CQDs-Ethanol, PEG-Ethanol (Type II), two component solutions including rC-Ethanol, rP-Ethanol, CP-Ethanol (Type III), and finally, the three-component solution rCP-Ethanol (Type IV).

addition, we created two-component solutions by mixing each of the two components in pure ethanol. Specifically, we mixed rGO-Ethanol and CQDs-Ethanol to create the rC-Ethanol solution, rGO-Ethanol and

PEG-Ethanol to create the rP-Ethanol solution and CQDs-Ethanol and PEG-Ethanol to create the CP-Ethanol solution (Type III). Finally, the rCP-Ethanol solution is created by mixing all three components (Type

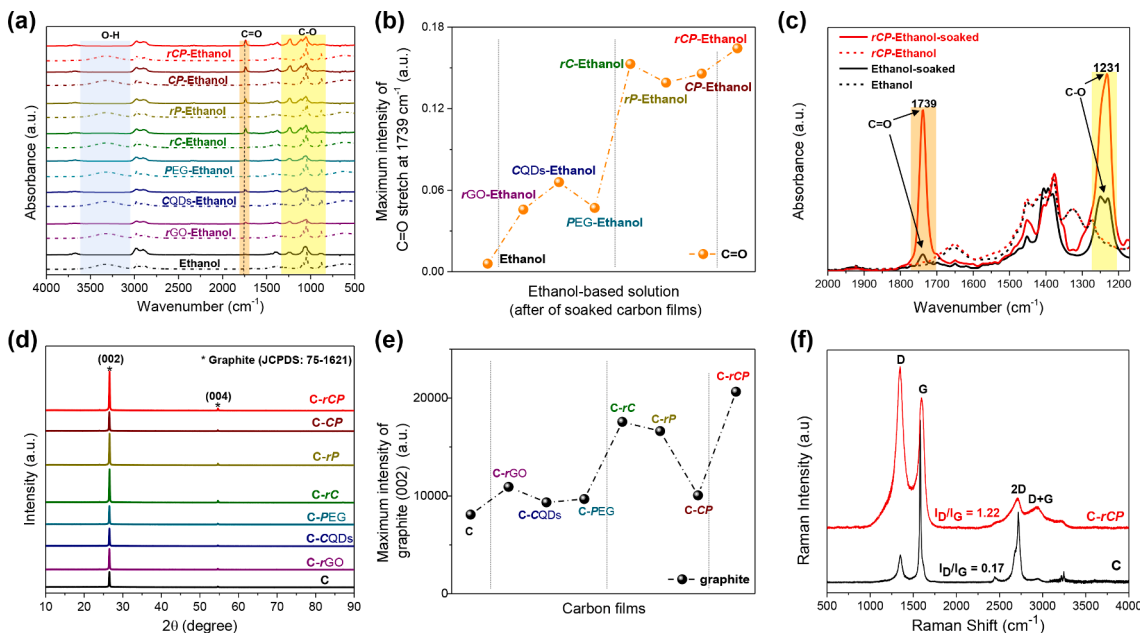


Fig. 2. (a) FTIR spectra of different ethanol-based solutions (dashed line: before, solid line: after soaking carbon films). (b) Maximum intensity of $\text{C}=\text{O}$ stretch at 1739 cm^{-1} with different ethanol-based solutions (after soaking carbon films). (c) FTIR spectra of $\text{C}=\text{O}$ and $\text{C}-\text{O}$ stretch before and after soaking the carbon films with the ethanol and rCP-Ethanol solutions. (d) XRD patterns and (e) Maximum intensity of graphite (002) of different carbon films. (f) Raman spectra of C and C-rCP films.

IV), as shown in Fig. 1c.

Fig. 2a presents the FTIR spectra of the ethanol-based solutions before and after the soaking of the carbon films. The peaks at around 1231 and 1739 cm⁻¹ indicate the presence of C-O and C=O functional group, respectively, in the soaked ethanol-based solutions, indicating the removal of some binders, particularly polar solvents, by the solvent interlacing method [36,57]. The soaked rCP-Ethanol solution shows a higher intensity of the C=O stretch peak at around 1739 cm⁻¹ than the other soaked ethanol-based solutions, as shown in Fig. 2b, indicating its superior ability to remove excess polar binders from the carbon films. This observation suggests that the rCP-Ethanol solution is the optimal choice for this application. Fig. 2c provides a clear visualization of the C=O and C-O stretch peaks of the ethanol and rCP-Ethanol solutions, before and after soaking the carbon films, confirming that the rCP-Ethanol solution is more effective solvent for removing the binder compared to ethanol. As a result of the superior performance of the rCP-Ethanol solution in removing the binder, the decision was made to graft the C-rCP films with the rCP composites in this study. Furthermore, Fig. 2d shows the X-ray diffraction (XRD) patterns of different carbon films, including C, C-rGO, C-CQDs, C-PEG, C-rC, C-rP, C-CP and C-rCP, which were named based on the different solutions used for soaking the carbon films. The XRD of each carbon film indicate its level of crystallinity, with the maximum

peak at $2\theta = 26.60^\circ$ representing the (002) plane and the minimal peak at $2\theta = 53.81^\circ$ representing the (004) planes of hexagonal graphite phase (JCPDS file no: 75-1621) [58]. Notably, the C-rCP films exhibit the highest XRD spectra, suggesting a higher density of carbon particles. Fig. 2e displays the maximum intensity of graphite (002) in the carbon films with different solvent interlacing solutions, supporting the exceptional conductivity of the C-rCP films which contain the highest amount of graphite. Raman spectroscopy was performed to investigate the surface components and crystal quality of the carbon films: C and C-rCP. As shown in Fig. 2f, both carbon films exhibited well-defined D and G bands, located at 1345 cm⁻¹ and 1595 cm⁻¹, respectively, indicating the typical properties of graphene. The D band is attributed to the structural defect of hexagonal graphitic layers in the plane C=C (carboxylic functional group), while the G band is related to the sp² carbon-type structure [59]. The peak intensity I_D/I_G ratio was calculated to evaluate the degrees of defects and disorder, and it was found to be higher in the C-rCP film (1.22) than in the C film (0.17), suggesting that the C-rCP films were grafted into the carbon paste with rCP composites, leading to an improvement in the reduction of defect in carbon film [60, 61]. Furthermore, the Raman spectra showed second-order characteristic peaks corresponding to the 2D and D+G bands at 2715 cm⁻¹ and 2937 cm⁻¹, respectively. This indicates that the amide, hydroxyl and

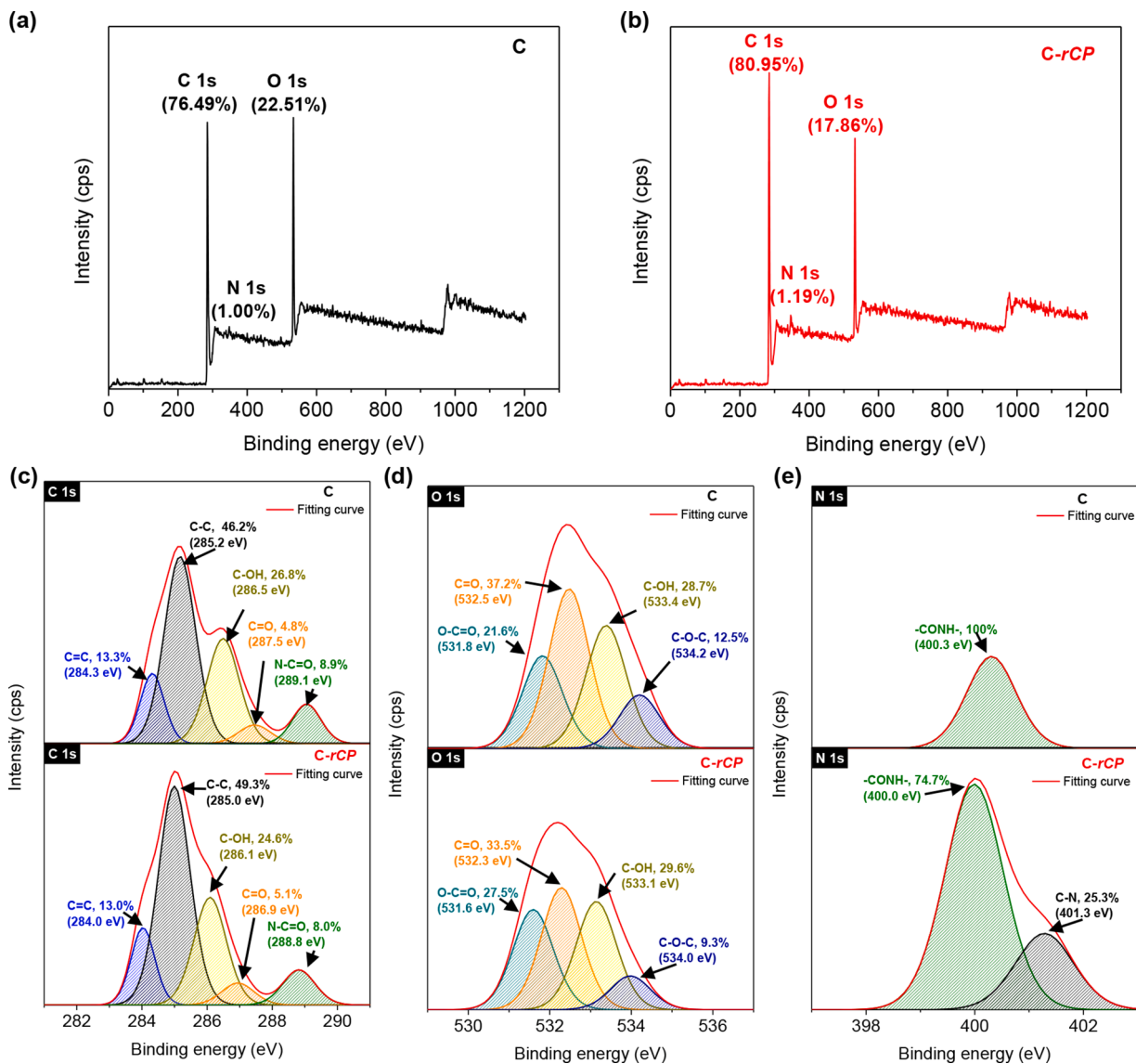


Fig. 3. (a,b) XPS survey spectra of C and C-rCP films. High resolution XPS spectra of C and C-rCP films for: (c) C1s, (d) O1s and (e) N1s, respectively.

carboxylic functional groups are predominant in the coffee ground-CQDs [62–64] and *r*GO-PEG composites [65]. These results confirm the existence of grafted *rCP* composites in the C-*rCP* films using the *rCP*-Ethanol solvent interlacing method. Overall, these findings suggest that the use of *rCP* composites in the carbon paste can improve the crystal quality and reduce the defects in carbon films.

X-ray photoelectron spectroscopy (XPS) analysis was performed on both C and C-*rCP* films to elucidate the surface chemical state and composition. The XPS survey spectra of the carbon films as shown in Fig. 3a,b, showed the percentages of C, O and N content, which were summarized in Table 1. As seen in Fig. 3c, the deconvoluted XPS C1s spectra of the C and C-*rCP* films presented several peaks centered at ~284, ~285, ~286, ~287 and ~289 eV, corresponding to C=C, C-C, C-OH, C=O, and N-C=O groups, respectively. The C component in the C-*rCP* films (80.95 at%) was found to be significantly higher value than that of the C films (76.49 at%). This indicates that there was a larger quantity of carbon particles grafted with the *rCP*-composites present in the C-*rCP* films, leading to the higher density of the carbon films. The deconvoluted XPS O1s spectra of the C and C-*rCP* films (Fig. 3d) exhibited four major peaks at ~531, ~532, ~533, and ~534 eV, attributed to O-C=O, C=O, C-OH, and C-O-C groups, respectively [66]. The XPS analysis showed that the C-*rCP* films had a lower oxygen concentration (17.86 at%) compared to the C film (22.51 at%), indicating that the polar solvent in the binder corresponding to the *rCP*-Ethanol solution preferred to remove oxygen bonds after soaking carbon films. This is consistent with the FTIR results (Fig. 2c). In addition, Fig. 3e demonstrated the deconvoluted XPS N1s spectra of the C and C-*rCP* films. The peak observed at ~400.3 eV in the XPS N1s spectra of the C films corresponds to the -CONH functional group. While the C-*rCP* films reveals an additional peak at ~401.3 eV, corresponding to -CN bonding (graphitic N groups). The presence of -CN peak in the XPS N1s spectra indicates that the nitrogen atoms from the coffee ground waste-CQDs were successfully incorporated into the C-*rCP* films, resulting in the formation of graphitic N groups [64]. This finding is consistent with the higher N content observed in the C-*rCP* films (1.19 at%) compared to the C (1.00 at%) [67]. This result is well-agreement with the XRD and Raman measurements, which also showed difference between the two types of carbon films.

The morphology of the different types of carbon films was investigated using scanning electron microscopy (SEM), and the results are shown in Figs. 4 and S4 (Supplementary material). The SEM images reveal remarkably different surface morphologies for each carbon film with distinct differences in density and homogeneity (Fig. S4a, Supplementary material). The C films (Fig. 4a) contain a lot of macro-porous gaps that are a result of the ethanol solvent-interlacing process, which dissolved the binders in the carbon paste [36,59]. In contrast, the C-*rCP* films (Fig. 4b) appear to be denser and more homogeneous. This is likely due to the ability of the *rCP* composites to embed into the macro-porous gaps between the graphite and carbon black in the carbon paste, filling in the gaps and creating a more uniform film. It appears that the addition of *rCP* composites to the carbon paste has improved the density and homogeneity of the resulting films, as the *rCP* can be grafted into the macro-porous gaps of the carbon paste, leading to closer contact between the carbon particles and a decrease in the size and density of the porosity. This improved contact between the carbon particles could enhance the electrical conductivity and mechanical stability of the resulting film, which may be beneficial for various applications. In addition, it seems that the heat-press transfer

method has been used to improve the adherence of the carbon films to the underlying layers. This is likely due to the thermo-plasticity of the polymer binders in the carbon paste, which allows them to soften and fuse together when subjected to heat and press during the transfer process. This can help to create a stronger bond between the carbon films and the substrates. The cross-section SEM results (Fig. 4c,d) may provide further evidence of the improved adherence of the carbon films to the underlying layers, as well as the reduced porosity and improved density of the resulting films. It can be clearly seen that, the thickness of C-*rCP* films is about 35 μm which is lower than the thickness of C films (~ 42 μm) by about 7 μm. The difference in thickness may be attributed to the ability of the *rCP* composites to embed into the macro-porous gaps of the carbon paste, resulting in a more compact film. The magnified cross-section SEM images of the C-PSC structures with different carbon films shown in Fig. 4c,d (right insets) provide further insight into the structure and properties of these films. The C device exhibits visible gaps between the spiro-OMeTAD/C interface, which can result in poor interface contact and charge recombination. Meanwhile, the C-*rCP* device reveals more self-adhesiveness and better interface contact between the spiro-OMeTAD/C-*rCP*, indicating that the addition of *rCP* composites to the carbon paste may improve the interface contact and overall performance of the device. To further demonstrate the beneficial bridging between the HTL and carbon films, the structure of FTO/spiro-OMeTAD with different carbon films were compared, as shown in Fig. S4b (Supplementary material). As a result, the C-*rCP* film shows a much better interfacial bridging effect compared to other carbon films. This can be attributed to the unique morphology of the *rCP* composites, which serve as bridging materials that greatly enhance the interfacial contact and charge extraction between the HTL and carbon films.

The AFM topological images in Fig. 5a demonstrated a root-mean-square surface roughness (RMS) of 169.13 and 127.87 nm for the C and C-*rCP* films, respectively. The surface roughness results obtained with the AFM step profiler for of both carbon films are presented in Fig. 5b. It is evident that the lateral surface roughness of the C-*rCP* films (315.6 nm) is significantly lower than the C films (565.2 nm), by around 250 nm. Generally, the surface roughness increased as the porosity of the films increased [35]. The analysis of surface roughness indicates that the C-*rCP* films are smoother, which can be attributed to the grafted *rCP* composites and the resulting increased density and wettability on the surface. The contact angle of water deposited on the C-*rCP* films is 80.16°, which is lower than the C film (90.21°), as shown in Fig. 5c. This demonstrates that the hygroscopic property of PEG permits the *rCP* composites to absorb water molecules on the C-*rCP* surface, preventing further erosion of the PSC devices with polar groups [34,68,69]. Therefore, the *rCP* grafted onto the carbon surface acts as a barrier, protecting the underlying layers of the PSC from direct exposure to moisture. By using *rCP*-treated carbon, the overall stability of PSCs can be improved, resulting in a longer lifetime. Additionally, the improvement in surface roughness of the C-*rCP* films could play an important role in the interaction between the spiro-OMeTAD/carbon interface. The smooth and self-adhesive nature of the C-*rCP* films offer a beneficial option for pressing on top of the HTL to reduce interfacial resistance and encourage charge transfer [35,46]. The mechanical flexibility tests of the different carbon films are shown in Fig. 5d,e. Both carbon films could droop naturally under the force of gravity, but the bending degree of the C-*rCP* films (55.3°) was greater than the C films (75.1°). This suggests that the C-*rCP* films have better flexibility and may have potential application in C-FPSCs devices [70,71]. The improved flexibility of the C-*rCP* films can be attributed the interlacing and grafting of the *rCP*-Ethanol solution into the carbon framework. In addition, when the C-*rCP* films were directly pressed on top of the HTL, their superior flexibility allowed for a better adhesion.

The electrical characteristics of the carbon films were determined using four-point probe resistivity measurements. Table 2 presents the thickness and sheet resistance of both C and C-*rCP* films in a 1 cm² area

Table 1
XPS analysis of the C and C-*rCP* films providing the atomic percentages (at%) for the C, O, N content.

Carbon film	C	O	N
C	76.49	22.51	1.00
C- <i>rCP</i>	80.95	17.86	1.19

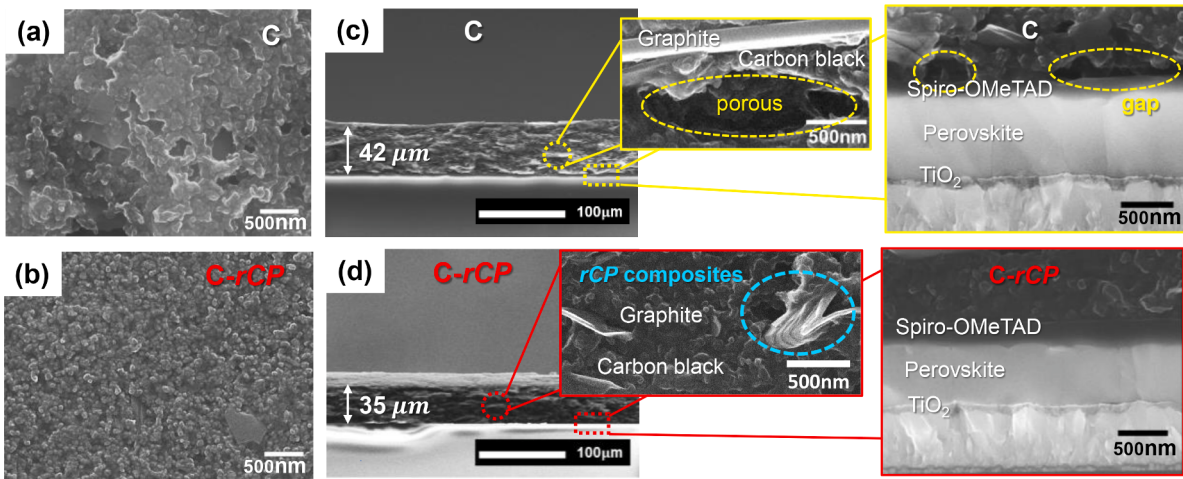


Fig. 4. (a,b) Top-view SEM images of C and C-rCP films. (c,d) Cross-sectional SEM images of C-PSCs using C films and C-rCP films as electrodes. Magnified cross-sectional images: C devices with macro-porous gaps between the graphite and carbon black (top-right insets: zoom-in image of the selected area) and C-rCP devices with rGO-CQDs-PEG composites that completely filled gaps between the graphite and carbon black (bottom-right insets: zoom-in image of the selected area).

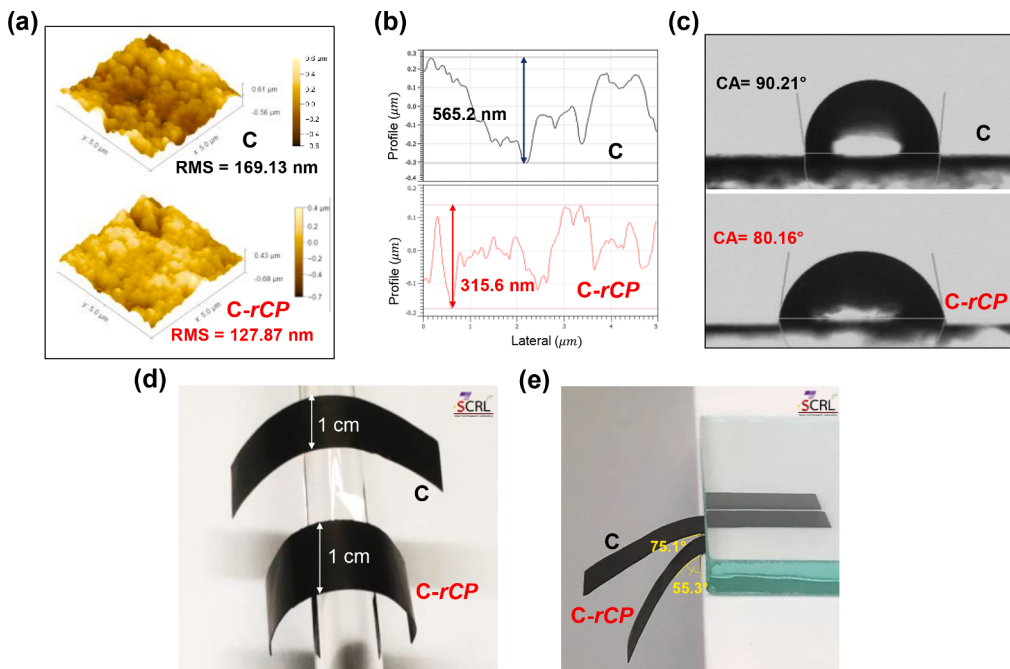


Fig. 5. (a) AFM topological images of C and C-rCP films. (b) AFM step profile images of C and C-rCP surfaces. (c) Contact angle of water deposited on C and C-rCP films. The mechanical flexibility of C and C-rCP films with natural drooping under the force of gravity: (d) top view and (e) side view.

Table 2

The thickness and sheet resistance of C and C-rCP films in an area of 1.00 cm² before and after heat pressing at 50 °C and a constant pressure of 0.6 Mpa.

Carbon film	Thickness (μm)		Sheet resistance (Ω square ⁻¹)	
	Before press	After press	Before press	After press
C	90.73 ± 3.45	42.52 ± 1.21	83.43 ± 8.74	13.20 ± 1.25
C-rCP	81.74 ± 2.23	35.17 ± 0.95	51.04 ± 3.53	6.13 ± 0.79

before and after heat pressing at 50 °C and a constant pressure of 0.6 MPa. The results indicate that the sheet resistance of the C-rCP films after heat pressing is the lowest, at approximately 6.13 Ω square⁻¹, with a corresponding thickness of about 35 μm. Therefore, heat-pressed C-rCP films are the most suitable choice for use as top electrodes in C-PSCs and

C-FPSCs.

To clearly understand the interface properties of the HTL and carbon films, the FTO/spiro-OMeTAD/carbon films devices were observed via direct current (DC) current–voltage (I-V) measurements with the carbon area of 1.00 cm². The device structure and the I-V curve are illustrated in Fig. 6a, and devices with different carbon films were compared. The results showed that both devices exhibited linear I-V characteristics, but the C-rCP devices perform the ohmic behavior better than the C devices. Moreover, the C-rCP devices had the best ohmic contact between the spiro-OMeTAD and the carbon interface when compared with other devices, as supported by the cross-section SEM results in Figs. S4b and S5, **Supplementary material**. The assumption behind this ohmic contact is that charge transport occurs across the carbon and underlayer. As a result, it can be claimed that the interface properties have a significant role to play in charge transport across interfaces, which impacts PSC

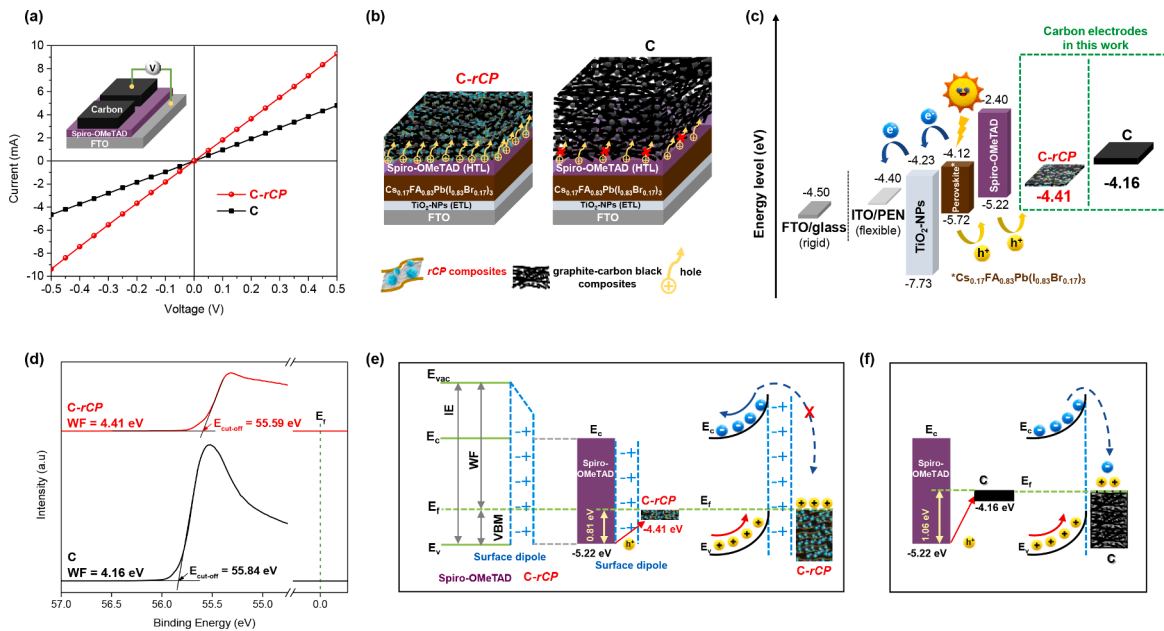


Fig. 6. (a) Schematic diagram and DC I - V curves of FTO/spiro-OMeTAD/different carbon electrodes. (b) Schematic representation of hole extraction and transport at the HTL/Carbon interface for C-PSCs with different carbon electrodes. (c) Energy level diagram of the PSC devices investigated in this work. (d) Ultraviolet photoelectron spectroscopy (UPS) spectra ($E_{\text{photon}} = 60 \text{ eV}$) at the secondary electron cutoff ($E_{\text{cut-off}}$) region and corresponding WF calculations of different carbon films. Schematic illustration of the energy level diagram of the HTL/Carbon interface: (e) spiro-OMeTAD/C-rCP and (f) spiro-OMeTAD/C.

device performance. In the fabrication of PSC devices, first the FTO (glass substrate) and ITO (PEN substrate) / TiO_2 -NPs/ $\text{Cs}_{0.17}\text{FA}_{0.83}\text{Pb}(\text{I}_{0.83}\text{Br}_{0.17})_3$ /spiro-OMeTAD were fabricated, then the different carbon films were directly heat-pressed on top of the spiro-OMeTAD layer. Fig. 6b provides schematic representations of hole extraction and hole transport at the HTL/Carbon interface for C and C-rCP PSC devices. According to the corresponding cross-sectional SEM images as shown in Fig. 4(c-d right insets), the HTL/C-rCP electrodes interface shows better contact with lower thickness. As described earlier, the C devices exhibit some obvious gaps between the HTL and carbon electrodes that result in a poor interface, charge recombination. Thanks to the improvement of the C-rCP electrodes, the macro-porous gaps between the graphite and carbon black in the carbon paste were grafted with the rCP composites, which caused the carbon particles to be in closer contact and significantly increased the density while reducing the porosity. To provide a better understanding of the energy level diagram of the PSC devices, Fig. 6c was presented, which includes the work function (WF) of each carbon films. To apply these carbon electrodes in PSCs, ultraviolet photoemission spectroscopy (UPS) measurement was performed and the results were shown in Figs. 6d and S6 (Supplementary material). The WF of the carbon electrode was calculated using Eq. (1) [72]

$$\text{WF} = 60.0 - E_{\text{cutoff}} \quad (1)$$

The WF values of C-rCP electrode and C electrode were determined to be 4.41 and 4.16 eV, respectively, indicating that the C-rCP electrode is more suitable for application in PSCs. The increase in WF of the C-rCP electrode is likely due to the formation of surface dipoles, resulting from the semiconductor behavior of the rGO [73] and the strongly polarized of -CN bonding in the coffee-CQDs [74], which could create the dipole moments at the surface of the C-rCP electrode. Moreover, the energy level mismatch between the spiro-OMeTAD and the carbon electrode was calculated by subtracting the ionization energy (IE) value of the spiro-OMeTAD (5.22 eV) [75,76] from the WF values of the carbon electrodes. The results show that the energy level mismatch of the spiro-OMeTAD/C-rCP electrode decreased to 0.81 eV, while it increased to 1.06 eV for that of the spiro-OMeTAD/C electrode. This reduction in energy level mismatch is expected to improve charge transfer and enhance the performance of PSC devices [77]. Furthermore, Fig. 6e,f

show schematic illustrations of the energy levels at the spiro-OMeTAD/different carbon interfaces. At the heterojunction of the spiro-OMeTAD layer and the carbon electrode, a significant Fermi level offset would produce a Schottky barrier and cause band bending [24,76, 77]. By performing interfacial engineering with rCP composites (Fig. 6e), an upward band bending can be achieved, which could increase carrier transport and prevent charge recombination [78]. This effect could be beneficial for improving the overall performance of PSC devices. Due to the appropriate energy level alignment between the spiro-OMeTAD and the C-rCP electrodes, along with their exceptional hole extraction ability and increased number of conduction routes, allow for efficient extraction of holes from the valence band of the spiro-OMeTAD to the C-rCP electrodes after the extraction generation. This in turn, enhances the extraction of electrons from the perovskite layer to the TiO_2 -NPs layer, leading to improved hole-electron separation and reduced charge recombination [79,80]. These results support the use of C-rCP as the top electrode in PSCs, as it can serve dual functions by acting as a bridge to connect the HTL/Carbon and providing high conductivity electrodes suitable for use in conventional structure C-PSC and C-FPSC fabrication, as seen in Fig. S7 (Supplementary material).

To demonstrate the performance of PSCs based on different carbon electrodes, the photovoltaic parameters of both rigid (C-PSC) and flexible (C-FPSC) devices with C and C-rCP electrodes were analyzed. The photovoltaic parameters include the power conversion efficiency (PCE), open circuit voltage (V_{oc}), short circuit current density (J_{sc}), and fill factor (FF) of the 16 cells with an active area of 0.04 cm^2 under 1 sun (AM 1.5G, irradiance of 100 mW cm^{-2}) illumination. The results, summarized in Fig. 7a and Table 3, indicate the photovoltaic performance of the C-rCP devices was higher than that of the C devices, as shown in Fig. 7b, which was expected due to the superior properties of the C-rCP electrodes. The best-performing C-PSC device fabricated on rigid substrates achieved a PCE of 15.40%, V_{oc} of 1.01 V, J_{sc} of 21.24 mA cm^{-2} and FF of 71.46%. Surprisingly, the best C-rCP PSC device fabricated with the electrodes demonstrated even better performance, with a PCE of 18.32%, V_{oc} of 1.03 V, J_{sc} of 22.35 mA cm^{-2} and FF of 79.81%. Further demonstration of utilizing carbon film electrodes in flexible devices was carried out with the fabrication of the C-FPSC devices (Fig. 7c), which achieved a best performance with a PCE of 10.19%, V_{oc}

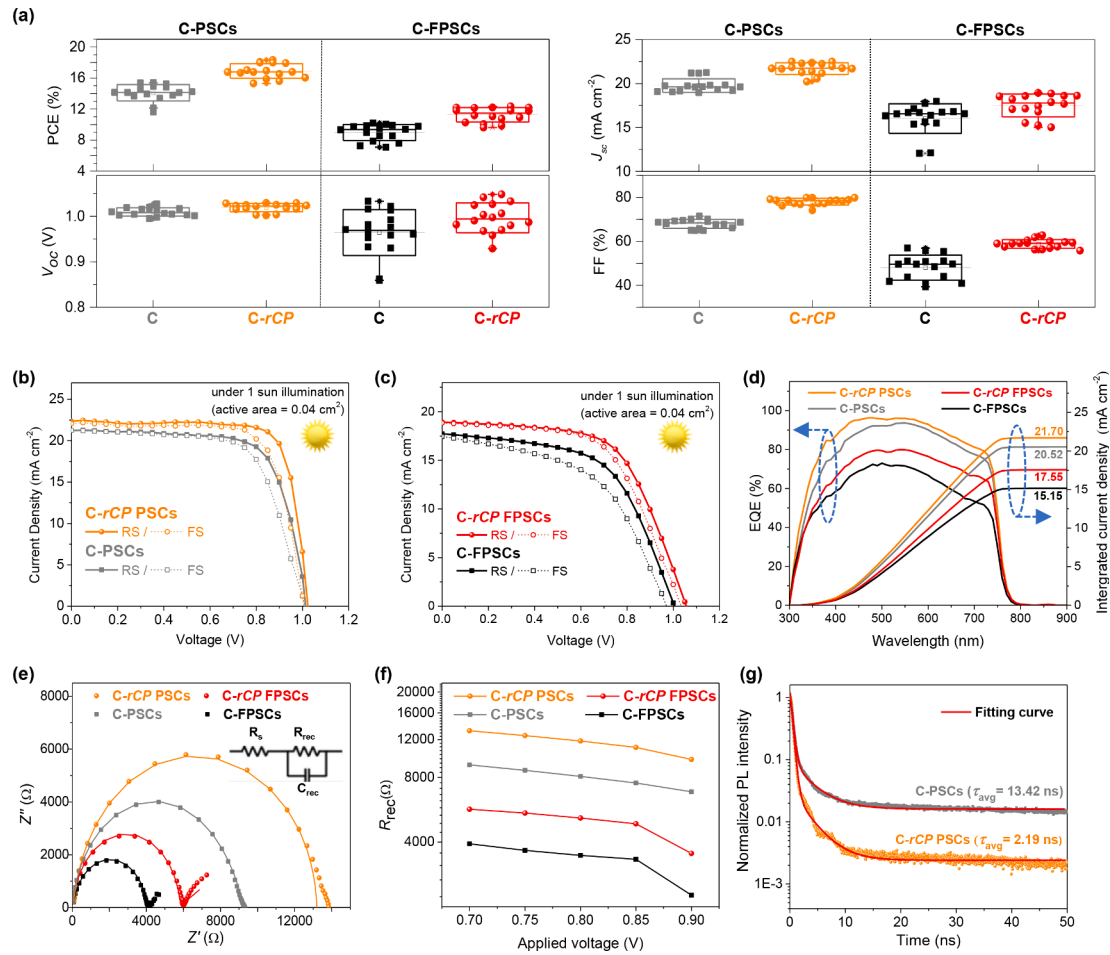


Fig. 7. (a) statistical photovoltaic parameters (PCE, V_{oc} , FF and J_{sc}) of rigid (C-PSC) and flexible (C-FPSC) devices based on C and C-rCP as electrodes (16 subcells) and Current density–voltage (J –V) characteristics of the champion (b) C-PSCs and c) C-FPSCs with an active area of 0.04 cm^2 under 1 sun (AM 1.5G, irradiance of 100 mW cm^{-2}) illumination. (d) EQE spectra and integrated current density (J_{int}) of different PSCs. (e) Nyquist plots with the equivalent circuit (as shown in inset) of different PSCs with an applied bias voltage of 0.7 V under dark with a carbon area of 0.16 cm^2 (solid symbols are original data and solid lines are fitted data). (f) Recombination resistance (R_{rec}) of different PSCs obtained with fitting Nyquist plots. g) Time-resolved photoluminescence decay (TRPL) spectra of FTO/TiO₂-NPs/Perovskite/Spiro-OMeTAD/different carbon electrodes (a 405 nm laser is incident from the FTO glass side).

Table 3

Statistical photovoltaic parameters of laboratory-scale rigid (C-PSC) and flexible (C-FPSC) devices with C and C-rCP electrodes based on 16 cells with an active area of 0.04 cm^2 under 1 sun (AM 1.5G, irradiance of 100 mW cm^{-2}) illumination.^{a)}

PSCs (0.04 cm^2)	V_{oc} (V)	J_{sc} (mA cm^{-2})	FF (%)	PCE (%)	R_s ($\Omega \text{ cm}^2$)	EQE J_{int} (mA cm^{-2})
C-PSCs	$1.01 (1.01 \pm 0.01)$	$21.24 (19.77 \pm 0.55)$	$71.46 (67.95 \pm 1.68)$	$15.40 (14.09 \pm 0.75)$	$2.80 (4.14 \pm 0.72)$	20.52
C-rCP PSCs	$1.03 (1.02 \pm 0.01)$	$22.35 (21.07 \pm 0.49)$	$79.81 (78.07 \pm 1.18)$	$18.32 (16.91 \pm 0.73)$	$2.47 (2.89 \pm 0.26)$	21.70
C-FPSCs	$1.01 (0.96 \pm 0.04)$	$17.73 (16.01 \pm 1.18)$	$56.95 (48.04 \pm 4.74)$	$10.19 (8.97 \pm 0.87)$	$9.28 (10.54 \pm 0.71)$	15.15
C-rCP FPSCs	$1.04 (1.00 \pm 0.03)$	$18.92 (17.51 \pm 1.04)$	$62.74 (58.80 \pm 1.55)$	$12.34 (11.23 \pm 0.79)$	$7.34 (7.72 \pm 0.34)$	17.55

^{a)} The average values are presented in parentheses.

of 1.01 V , J_{sc} of 17.73 mA cm^{-2} , and FF of 56.95% . However, C-rCP FPSC devices fabricated with the same carbon electrodes outperformed C-FPSC devices, recording a best performance with a PCE of 12.34% , V_{oc} of 1.04 V , J_{sc} of 18.92 mA cm^{-2} , and FF of 62.74% . Clearly, all the photovoltaic parameters (PCE, V_{oc} , J_{sc} and FF) were improved for the C-rCP devices compared to the C devices (Table 3). The improved FF value observed in the C-rCP devices was mainly attributed to the beneficial interface contact between the spiro-OMeTAD and C-rCP electrode, which has a significant impact on charge transport across interfaces and the overall performance of PSC devices. As shown in Fig. 7d, the charge transfer ability of the C-rCP devices was compared to the C devices using the external quantum efficiency (EQE) measurement in the active area of 0.04 cm^2 . High EQE values recorded by the C-rCP devices were in the

wavelength range between 400 and 750 nm . The corresponding integrated current density (J_{int}) values (Table 3) also confirmed the improved charge transfer ability in the C-rCP devices (achieved EQE J_{int} of 21.70 and 17.55 mA cm^{-2} in rigid and flexible devices, respectively). These J_{int} values were in acceptable agreement with the J_{sc} values obtained from J –V measurement under AM 1.5G conditions. This higher EQE in the C-rCP devices would be a result of the better charge transfer ability due to the superior spiro-OMeTAD/carbon interface interaction as discussed above. These results confirm that the C-rCP electrodes could improve the performance of the devices. To investigate the charge carrier mechanism of the PSCs, the electrochemical impedance spectroscopy (EIS) was performed. The Nyquist plots of the experimental data (as shown in Fig. 7e), obtained with an applied bias voltage of 0.7 V

under dark and a carbon area of 0.16 cm^2 were fitted using the equivalent circuit to extract series resistance (R_s) and recombination resistance (R_{rec}) values. The results indicated that both rigid and flexible C-rCP devices exhibited higher curve diameters and higher R_{rec} values than the C devices. The carrier R_{rec} values of the C-PSCs were measured at an applied bias of 0.7, 0.75, 0.8, 0.85, and 0.9 V and are exhibited in Fig. 7f. It can be seen that the R_{rec} of the C-rCP devices is dramatically higher than the C devices. These results confirmed the reduction of charge recombination in the C-rCP devices. To further investigate the charge transfer dynamics, time-resolved photoluminescence decay (TRPL) at $\sim 760 \text{ nm}$ was measured for each device using a pulsed diode laser of 405 nm and illuminated from the FTO glass side [39,81]. The TRPL decay reflects the charge transfer across the entire device [82]. The normalized TRPL spectra of different devices are shown in Fig. 7g, the TRPL fitting parameters obtained using a bi-exponential decay function (Eq. (2)) [77,81–83] are listed in Table S1 (Supplementary material)

$$f(t) = A_1 \exp(-t/\tau_1) + A_2 \exp(-t/\tau_2), \quad (2)$$

where A_1 and A_2 are the decay amplitudes with lifetimes τ_1 and τ_2 , respectively. The average lifetimes (τ_{avg}) can be estimated by Eq. (3) [77,81]

$$\tau_{\text{avg}} = A_1 \times \tau_1 + A_2 \times \tau_2 \quad (3)$$

The C-rCP device exhibited a lower charge recombination lifetime, with a normalized τ_{avg} of 2.19 ns, compared to the C devices, which had a normalized τ_{avg} of 13.42 ns. This indicates that the C-rCP device had faster charge transfer, which is attributed to the modulation of energy level alignment through the addition of rCP-composites to carbon film. This led to decrease the charge recombination between the HTL and carbon electrode, resulting in proper hole extraction and enhanced device performance. When compared to other carbon electrodes on rigid substrates (Fig. S8 and Table S2, Supplementary material), the C-rCP devices exhibited the best performance with PCEs of 18.32%, 17.33, 15.52 and 12.70% with active areas of 0.04, 0.09, 0.16 and 1.00 cm^2 ,

respectively. This demonstrates that the C-rCP film had the greatest interfacial engineering with the rCP composites, which improved conductivity and led to a softness-based favorable interface contact between the carbon electrodes and the underlying layers. These findings are supported by the EQE, EIS and TRPL results. To verify the positive effect by rCP constituent, the photovoltaic performance of the C-PSCs fabricated by the additive engineering (C@rCP), i.e., adding the rCP directly into the commercial carbon paste, and the surface passivation by the ethanol solvent interlacing process (C-rCP) were compared to C electrodes as shown in Fig. S9 and Table S3 (Supplementary material). It clearly exhibits that the surface passivation strategy (C-rCP) obtaining 18.32% PCE is more favorable than the additive engineering for C@rCP devices (16.29% PCE) and the C devices (15.40% PCE). The results confirm that the introduction of rCP constituent can enhance crystallinity and reduce the defects in carbon films, which should benefit from the efficient charge extraction at the HTL/carbon films interface, leading to a significant increase in the FF and PCE of devices. However, the additive engineering (C@rCP) in the commercial carbon paste needs to be clarified and solved in future research.

For large-scale devices, Fig. 8a and Table 4 present the photovoltaic parameters of C-PSC and C-FPSC devices with C and C-rCP electrodes based on 12 cells having an active area of 1.00 cm^2 under 1 sun (AM 1.5G, irradiance of 100 mW cm^{-2}) illumination. As shown in Fig. 8b, the champion CPSC device recorded a performance with a PCE of 10.03%, V_{oc} of 1.08 V, J_{sc} of 17.45 mA cm^{-2} and FF of 53.22%. Moreover, the highest performing C-rCP PSC device recorded a performance with a PCE of 12.70%, V_{oc} of 1.09 V, J_{sc} of 19.42 mA cm^{-2} and FF of 60.05%. Furthermore, the large-scale C-FPSC devices (Fig. 8c) recorded the lowest performance parameters amongst the group of large-scale devices with a PCE of 6.43%, V_{oc} of 1.02 V, J_{sc} of 16.02 mA cm^{-2} and FF of 40.00%. Whereas, the greatest C-rCP FPSC devices recorded a performance with a PCE of 8.80%, V_{oc} of 1.03 V, J_{sc} of 17.18 mA cm^{-2} and FF of 50.35%. The results demonstrated that the performance parameters for the C-rCP devices were all significantly higher than for the C devices both for the rigid and flexible substrates due to significantly decreasing the R_s of the C-rCP devices, as shown in Table 3 and Table 4.

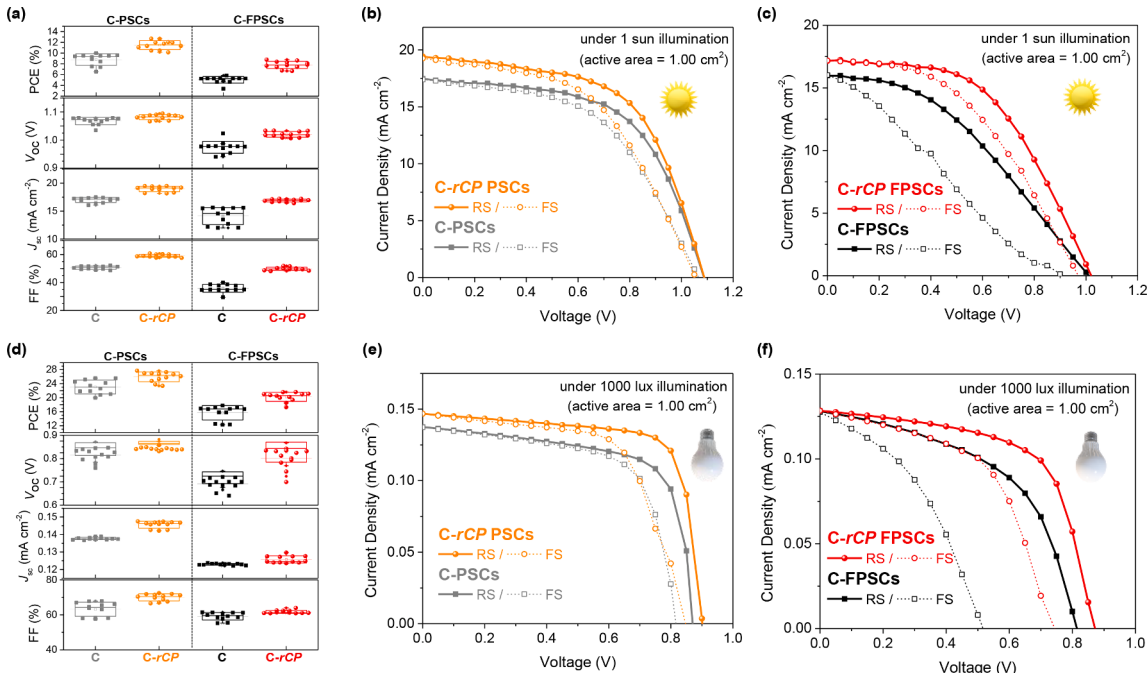


Fig. 8. (a) statistical photovoltaic parameters (PCE, V_{oc} , FF and J_{sc}) of different PSCs with C and C-rCP as electrodes (12 subcells) and J-V curves of champion (b) C-PSCs and (c) C-FPSCs with active area of 1.00 cm^2 under 1 sun (AM 1.5G, irradiance of 100 mW cm^{-2}) illumination. (d) statistical photovoltaic parameters of different PSCs with C and C-rCP electrodes (12 subcells) and J-V curves of champion (e) C-PSCs and (f) C-FPSCs with active area of 1.00 cm^2 under 1000 lux illumination.

Table 4

Statistical photovoltaic parameters of rigid (C-PSC) and flexible (C-FPSC) devices with C and C-rCP electrodes based on 12 cells in large-scale (1.00 cm^2) under 1 sun (AM 1.5G, irradiance of 100 mW cm^{-2}) illumination.^{a)}

PSCs (1.00 cm^2)	V_{oc} (V)	J_{sc} (mA cm^{-2})	FF (%)	PCE (%)	R_s ($\Omega \text{ cm}^2$)
C-PSCs	1.08 (1.07 ± 0.01)	17.45 (16.99 ± 0.39)	53.22 (50.56 ± 1.04)	10.03(8.71) (± 0.83)	20.73 (26.24 ± 1.51)
C-rCP PSCs	1.09 (1.08 ± 0.01)	19.42 (18.97 ± 0.35)	60.05 (59.11 ± 0.90)	12.70 (11.50 ± 0.68)	13.85 (15.23 ± 1.05)
C-FPSCs	1.02 (0.97 ± 0.01)	16.02 (14.11 ± 1.35)	40.01 (35.91 ± 2.22)	6.43 (5.04) (± 0.42)	29.28 (36.54 ± 14.71)
C-rCP FPSCs	1.03 (1.02 ± 0.01)	17.18 (16.90 ± 0.21)	50.35 (49.77 ± 0.84)	8.80(7.82) (± 0.52)	21.28 (23.28 ± 5.79)

^{a)} The average values are presented in parentheses.

Furthermore, The substantial enhancement of J_{sc} and FF was due to the reduction of the interface resistance at the HTL/carbon interface [84, 85]. The interface properties can be said to have a considerable impact on charge transport across interfaces and subsequently on PSC device performance. In addition, indoor application of both rigid and flexible large-scale devices were investigated. The photovoltaic performance of the C and C-rCP devices under low light conditions was characterized using $J-V$ measurement with an active area of 1.00 cm^2 under a cool daylight 6500 K LED light illumination with a light intensity of 1000 lux ($0.3175 \text{ mW cm}^{-2}$), as shown in Fig. S10 (Supplementary material). The photovoltaic parameters of the devices are summarized in Fig. 8d and Table 5. Moreover, the $J-V$ curves of the best performing large-scale C and C-rCP devices are demonstrated in Fig. 8e,f. It can be seen that considerable PCEs of 27.71% and 21.61% were achieved for rigid and flexible substrates, respectively, based C-rCP devices with an active area of 1.00 cm^2 , which were significantly higher than those of the C devices (25.58% with C-PSCs and 16.80% with C-FPSCs). The main PCE improvement was due to the enhancement in the FF value, which could be ascribed to the better charge transfer ability with the beneficial interface contact between the HTL and carbon electrodes, as mentioned above. The reason for the unexpected behavior of C-FPSCs in Fig. 8c,f is the lack of interface in the large-scale C-FPSC devices, leading to decreasing in both J_{sc} and FF of devices. However, C-rCP could solve this phenomenon due to the enhancement of the interface contact between the HTL and carbon electrodes. In future research, the interface issues that occur in the large-scale C-FPSCs needs to be defined and resolved. To evaluate hysteresis effects in the PSCs, JV curves were obtained under forward and reverse scans. A hysteresis index (HI) was calculated using the following Eq. (4) [43]:

$$\text{HI} = \frac{\text{PCE}_{rev} - \text{PCE}_{fw}}{\text{PCE}_{rev}}, \quad (4)$$

where PCE_{rev} is the PCE value collected under reverse scan, and PCE_{fw} is the PCE value collected under forward scan. The interfacial bridging with grafted rCP composites in the carbon films resulted in a negligible hysteresis effect, which was observed in both measurement under 1 sun and 1000 lux illumination, as shown in Table S4 and Table S5 (Supplementary material). In addition, the weight of the $2.0 \times 2.5 \text{ cm}^2$ flexible C-rCP device (0.1364 g , thickness of 0.242 mm) was significantly lighter than that of the rigid C-rCP device, with a weight reduction of about 20 times and thinner thickness (the rigid C-rCP device: 2.8122 g , thickness of 2.278 mm), as shown in Fig. S11 (Supplementary material). Additionally, the lightweight flexible C-rCP device achieved an outstanding specific power-per-weight of 0.323 W g^{-1} in comparison to the rigid C-rCP device (0.022 W g^{-1}). These results suggest that our flexible C-rCP devices have promising for future commercialization and up-scaling.

Enhancing long-term stability is crucial for the eco-commercial profitability of PSCs. Fig. 9a,b depicts the evolution of normalized PCE as well as the long-term stability performance of C-PSC and C-FPSC devices with C and C-rCP electrodes in active areas of 0.04 and 1.00 cm^2 . The long-term stability of the devices was tested under 1 sun (AM 1.5G, irradiance of 100 mW cm^{-2}) illumination in ambient air conditions ($\sim 25^\circ\text{C}$), 35–45 %RH without encapsulation based on ISOS-D1 protocol (kept in dark storage; room temperature; ambient humidity) and dedicated at T_{80} , which is the time passed during the ageing experiment to reach 80% of the initial PCE [86]. The C-PSCs and C-FPSCs based on the C-rCP electrodes both of small- and large-area retained superior long-term stability represented by maintaining more than 80% of their initial PCE for 1000 h. At the same time, the C devices displayed a long-term stability slightly lower than the C-rCP devices in the rigid substrates (small & large-area) and the C-FPSCs (small-area). However, the stability of a flexible C device in a large-scale was dramatically less since tests showed it retained 69% of the initial PCE after 1032 h. According to these results, the C-rCP electrodes not only enhance device performance but also activates a mechanism that prolongs the large-area flexible device lifecycle and delays device breakdown. This implies that the rCP composites in the C-rCP electrodes behave as a barrier for PSCs, preventing the spiro-OMeTAD or the perovskite layer degradation. To confirm the mechanical durability of the large-scale flexible devices, we conducted cyclic bending tests of flexible devices with a bending radius of 17 mm . As shown in Fig. 9c, the large-scale C-rCP FPSCs exhibited good mechanical stability, maintaining an average of 80% of the initial PCE after 1000 bending cycles, whereas the average PCE of C-FPSCs was dramatically decreased to 60% of its initial PCE after the same bending cycle. This indicates that the superior self-adhesive C-rCP electrode could be beneficial to release the bending stress in the perovskite and spiro-OMeTAD films, improving their mechanical stability.

4. Conclusions

In conclusion, a novel carbon film, C-rCP, was successfully prepared using a modified, room-temperature ethanol solvent interlacing process with a magnetic stirring. The process involved grafting rCP composites onto C-rCP films, which improves their conductivity and density. These films are suitable as top electrodes in C-FPSCs due to their lower sheet resistance and favorable energy band position, which enhance the HTL/carbon interface and therefore the charge transfer. The improved adhesion of the HTL/carbon was due to the higher density, excellent flexibility, suitable thickness and great self-adhesiveness of the C-rCP films. Notably, the rigid C-rCP devices achieved the best PCE of 18.34% in a small-area (0.04 cm^2) and 12.70% in a large-area (1.00 cm^2), while the flexible C-rCP devices recorded the best PCEs of 12.34% and 8.80% for small and large areas, respectively. Furthermore, the devices

Table 5

Statistical photovoltaic parameters of rigid (C-PSC) and flexible (C-FPSC) devices with C and C-rCP electrodes based on 12 cells in laboratory-scale (1.00 cm^2) under 1000 lux illumination.^{a)}

PSCs (1.00 cm^2)	V_{oc} (V)	J_{sc} (mA cm^{-2})	FF (%)	PCE (%)
C-PSCs	0.869 (0.840 ± 0.022)	0.1376 (0.1377 ± 0.0005)	67.86 (63.17 ± 3.43)	25.58 (23.05 ± 1.70)
C-rCP PSCs	0.882 (0.867 ± 0.005)	0.14786 (0.1456 ± 0.0015)	72.43 (69.98 ± 1.68)	27.71 (25.96 ± 1.13)
C-FPSCs	0.812 (0.718 ± 0.019)	0.1282 (0.1229 ± 0.0004)	51.26 (59.18 ± 1.78)	16.80 (15.68 ± 1.65)
C-rCP FPSCs	0.859 (0.828 ± 0.032)	0.1284 (0.1258 ± 0.0018)	63.96 (61.72 ± 0.72)	21.61 (20.24 ± 0.98)

^{a)} The average values are presented in parentheses.

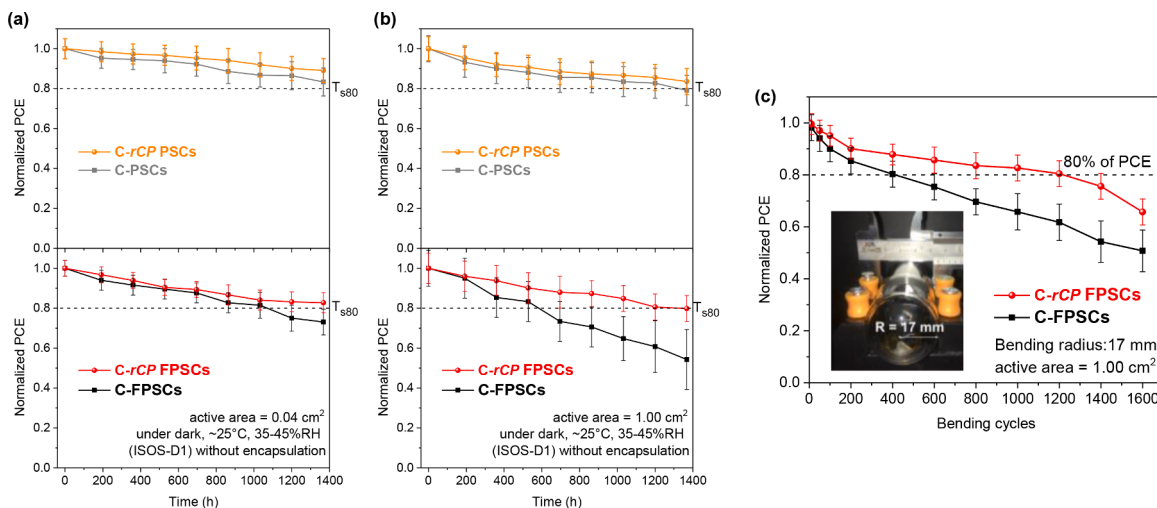


Fig. 9. Environmental and mechanical stability of PSCs. Normalized averaged PCE of rigid (C-PSC) and flexible (C-FPSC) devices with C and C-rCP electrodes of (a) 0.04 cm² (16 subcells) and (b) 1.00 cm² (12 subcells) stored under dark and ambient air conditions (~25 °C, 35–45%RH) without encapsulation (based on ISOS-D1, T_{s80} = the time passed during the ageing experiment to reach 80% of the initial PCE). (c) Normalized averaged PCE of C and C-rCP flexible devices with active area 1.00 cm² after bending durability tests with a bending radius of 17 mm for 1600 cycles (inset: bending test for C-FPSC device). Four devices were tested for each C and C-rCP condition.

retained long-term stability over 80% of their initial PCE for 1000 h in an ambient air environment without encapsulation. This research is the first report to introduce this rCP agent to C-FPSCs, offering an effective method towards up-scaling and future commercialization.

CRediT authorship contribution statement

Woraprom Passatorntaschakorn: Conceptualization, Methodology, Formal analysis, Investigation, Validation, Writing – original draft. **Warunee Khampa:** Investigation, Methodology. **Wongsathon Musikpan:** Investigation, Methodology. **Chawalit Bhoomanee:** Methodology. **Athipong Ngamjarurojana:** Validation. **Sakhorn Rimjaem:** Validation. **Atcharawon Gardchareon:** Validation. **Chatchai Rodwihok:** Investigation, Methodology, Validation. **Han S. Kim:** Validation. **Nutchai Khambunkoed:** Methodology. **Ratchadaporn Supruangnet:** Investigation, Validation. **Hideki Nakajima:** Validation. **Ladda Srathongsian:** Methodology. **Pongsakorn Kanjanaboons:** Validation. **Akarin Intaniwet:** Validation. **Anusit Kaewprajak:** Validation. **Pisist Kumnorkaew:** Validation. **Fabrice Goubard:** Validation. **Pipat Ruankham:** Investigation, Methodology, Validation, Writing – review & editing. **Duangmanee Wongratanaphisan:** Conceptualization, Supervision, Validation, Writing – review & editing.

Declaration of Competing Interest

The authors declare the following financial interests/personal relationships which may be considered as potential competing interests: Duangmanee Wongratanaphisan reports financial support was provided by National Research Council of Thailand.

Data availability

No data was used for the research described in the article.

Acknowledgments

This project is funded by National Research Council of Thailand (NRCT): (N41A650083). This research has received funding support from the NSRF via the Program Management Unit for Human Resources & Institutional Development, Research and Innovation [grant number

B40G660041]. The authors would like to acknowledge the support provided by Franco-Thai Cooperation Programme in Higher Education and Research/Franco-Thai Mobility Programme/PHC SIAM 2023, the Graduate School of Chiang Mai University and Thailand Center of Excellent in Physics. The authors would like to extend our gratitude to Assoc. Prof. Dr. Chesta Ratanaphan from Graphene Deep Tech (Thailand) Co., Ltd. for supplying the reduced graphene oxide (rGO) powder, Ravint Wongratanaphisan for synthesizing of Thai coffee ground waste-CQDs and Cynthia Bail for guidance with editing and proofreading in the English language. The authors thank all members of the Solar Cell Research Laboratory (SCRL) for their support and guidance in material preparation.

Supplementary materials

Supplementary material associated with this article can be found, in the online version, at [doi:10.1016/j.apmt.2023.101895](https://doi.org/10.1016/j.apmt.2023.101895).

References

- [1] A.K. Jena, A. Kulkarni, T. Miyasaka, Halide Perovskite photovoltaics: background, status, and future prospects, Chem. Rev. 119 (5) (2019) 3036–3103, <https://doi.org/10.1021/acs.chemrev.8b00539>.
- [2] F. Huang, M. Li, P. Siffalovic, G. Cao, J. Tian, From scalable solution fabrication of perovskite films towards commercialization of solar cells, Energy Environ. Sci. 12 (2) (2019) 518–549, <https://doi.org/10.1039/C8EE03025A>.
- [3] M. Petrović, V. Chellappan, S. Ramakrishna, Perovskites: solar cells & engineering applications – materials and device developments, Sol. Energy 122 (2015) 678–699, <https://doi.org/10.1016/j.solener.2015.09.041>.
- [4] A. Koijima, K. Teshima, Y. Shirai, T. Miyasaka, Organometal halide perovskites as visible-light sensitizers for photovoltaic cells, J. Am. Chem. Soc. 131 (17) (2009) 6050–6051, <https://doi.org/10.1021/ja809598r>.
- [5] M.M. Lee, J. Teuscher, T. Miyasaka, T.N. Murakami, H.J. Snaith, Efficient hybrid solar cells based on meso-superstructured organometal halide perovskites, Science 338 (6107) (2012) 643–647, <https://doi.org/10.1126/science.1228604>.
- [6] J. Burschka, N. Pellet, S.J. Moon, R. Humphry-Baker, P. Gao, M.K. Nazeeruddin, M. Grätzel, Sequential deposition as a route to high-performance perovskite-sensitized solar cells, Nature 499 (7458) (2013) 316–319, <https://doi.org/10.1038/nature12340>.
- [7] W.S. Yang, B.W. Park, E.H. Jung, N.J. Jeon, Y.C. Kim, D.U. Lee, S.S. Shin, J. Seo, E. K. Kim, J.H. Noh, S. Seok, Iodide management in formamidinium-lead-halide-based perovskite layers for efficient solar cells, Science 356 (6345) (2017) 1376–1379, <https://doi.org/10.1126/science.aan2301>.
- [8] H. Kim, K.G. Lim, T.W. Lee, Planar heterojunction organometal halide perovskite solar cells: roles of interfacial layers, Energy Environ. Sci. 9 (1) (2016) 12–30, <https://doi.org/10.1039/C5EE02194D>.
- [9] H. Min, D.Y. Lee, J. Kim, G. Kim, K.S. Lee, J. Kim, M.J. Paik, Y.K. Kim, K.S. Kim, M. G. Kim, T.J. Shin, S. il Seok, Perovskite solar cells with atomically coherent

- interlayers on SnO₂ electrodes, *Nature* 598 (7881) (2021) 444–450, <https://doi.org/10.1038/s41586-021-03964-8>.
- [10] K.L. Wang, Y.H. Zhou, Y.H. Lou, Z.K. Wang, Perovskite indoor photovoltaics: opportunity and challenges, *Chem. Sci.* 12 (36) (2021) 11936–11954, <https://doi.org/10.1039/D1SC03251H>.
- [11] P. Docampo, J.M. Ball, M. Darwich, G.E. Eperon, H.J. Snaith, Efficient organometal trihalide perovskite planar-heterojunction solar cells on flexible polymer substrates, *Nat. Commun.* 4 (1) (2013) 2761, <https://doi.org/10.1038/ncomms3761>.
- [12] M.H. Kumar, N. Yantara, S. Dharani, M. Graetzel, S. Mhaisalkar, P.P. Boix, N. Mathews, Flexible, low-temperature, solution processed ZnO-based perovskite solid state solar cells, *Chem. Commun.* 49 (94) (2013) 11089, <https://doi.org/10.1039/c3cc46534a>.
- [13] L. Li, Y. Wang, X. Wang, R. Lin, X. Luo, Z. Liu, K. Zhou, S. Xiong, Q. Bao, G. Chen, Y. Tian, Y. Deng, K. Xiao, J. Wu, M.I. Saidaminov, H. Lin, C.Q. Ma, Z. Zhao, Y. Wu, H. Tan, Flexible all-perovskite tandem solar cells approaching 25% efficiency with molecule-bridged hole-selective contact, *Nat. Energy* 7 (8) (2022) 708–717, <https://doi.org/10.1038/s41560-022-01045-2>.
- [14] L. Fagioli, F. Bella, Carbon-based materials for stable, cheaper and large-scale processable perovskite solar cells, *Energy Environ. Sci.* 12 (12) (2019) 3437–3472, <https://doi.org/10.1039/C9EE02115A>.
- [15] H. Yuan, E. Debroye, K. Janssen, H. Naiki, C. Steuwe, G. Lu, M. Moris, E. Orgiu, H. Uji-i, F. de Schryver, P. Samori, J. Hofkens, M. Roekaers, Degradation of methylammonium lead iodide perovskite structures through light and electron beam driven ion migration, *J. Phys. Chem. Lett.* 7 (3) (2016) 561–566, <https://doi.org/10.1021/acs.jpclett.5b02828>.
- [16] D. Bogachuk, S. Zouhair, K. Wojciechowski, B. Yang, V. Babu, L. Wagner, B. Xu, J. Lim, S. Mastrianni, H. Pettersson, A. Hagfeldt, A. Hinsch, Low-temperature carbon-based electrodes in perovskite solar cells, *Energy Environ. Sci.* 13 (11) (2020) 3880–3916, <https://doi.org/10.1039/D0EE02175J>.
- [17] I. Hwang, I. Jeong, J. Lee, M.J. Ko, K. Yong, Enhancing stability of perovskite solar cells to moisture by the facile hydrophobic passivation, *ACS Appl. Mater. Interfaces* 7 (31) (2015) 17330–17336, <https://doi.org/10.1021/acsami.5b04490>.
- [18] X. Meng, J. Zhou, J. Hou, X. Tao, S.H. Cheung, S.K. So, S. Yang, Versatility of carbon enables all carbon based perovskite solar cells to achieve high efficiency and high stability, *Adv. Mater.* 30 (21) (2018), 1706975, <https://doi.org/10.1002/adma.201706975>.
- [19] H. Chen, S. Yang, Carbon-based perovskite solar cells without hole transport materials: the front runner to the market? *Adv. Mater.* 29 (24) (2017), 1603994 <https://doi.org/10.1002/adma.201603994>.
- [20] Y. Yu, M.T. Hoang, Y. Yang, H. Wang, Critical assessment of carbon pastes for carbon electrode-based perovskite solar cells, *Carbon* 205 (2023) 270–293, <https://doi.org/10.1016/j.carbon.2023.01.046>.
- [21] A. Ghaffari, Z. Saki, N. Taghavina, M.M. Byranvand, M. Saliba, Lamination methods for the fabrication of perovskite and organic photovoltaics, *Mater. Horiz.* 9 (10) (2022) 2473–2495, <https://doi.org/10.1039/D2MH00671E>.
- [22] S. Suragkitthu, O. Tserendavag, U. Vandandoo, A.S.R. Bati, M. Bat-Erdene, J. G. Shapter, M. Batmunkh, S. Davaasambuu, Efficiency and stability enhancement of perovskite solar cells using reduced graphene oxide derived from earth-abundant natural graphite, *RSC Adv.* 10 (15) (2020) 9133–9139, <https://doi.org/10.1039/D0RA01423K>.
- [23] A.L. Palma, L. Cinà, S. Pescetelli, A. Agresti, M. Raggio, R. Paolesse, F. Bonaccorso, A. di Carlo, Reduced graphene oxide as efficient and stable hole transporting material in mesoscopic perovskite solar cells, *Nano Energy* 22 (2016) 349–360, <https://doi.org/10.1016/j.nanoen.2016.02.027>.
- [24] H. Tang, T. Xu, X. Qin, K. Zou, S. Lv, J. Fan, T. Huang, L. Chen, W. Huang, Carbon quantum dot-passivated perovskite/carbon electrodes for stable solar cells, *ACS Appl. Nano Mater.* 4 (12) (2021) 13339–13351, <https://doi.org/10.1021/acsnano.1c02850>.
- [25] S. Wang, P. Jiang, W. Shen, A. Mei, S. Xiong, X. Jiang, Y. Rong, Y. Tang, Y. Hu, H. Han, A low-temperature carbon electrode with good perovskite compatibility and high flexibility in carbon based perovskite solar cells, *Chem. Commun.* 55 (19) (2019) 2765–2768, <https://doi.org/10.1039/C8CC09905G>.
- [26] Q. Luo, H. Ma, Q. Hou, Y. Li, J. Ren, X. Dai, Z. Yao, Y. Zhou, L. Xiang, H. Du, H. He, N. Wang, K. Jiang, H. Lin, H. Zhang, Z. Guo, All-Carbon-Electrode-Based Endurable Flexible Perovskite Solar Cells, *Adv. Funct. Mater.* 28 (11) (2018), 1706777, <https://doi.org/10.1002/adfm.201706777>.
- [27] M. Que, B. Zhang, J. Chen, X. Yin, S. Yun, Carbon-based electrodes for perovskite solar cells, *Mater. Adv.* 2 (17) (2021) 5560–5579, <https://doi.org/10.1039/D1MA00352F>.
- [28] J. Zhang, G. Zhang, P. Su, R. Huang, J. Lin, W. Wang, Z. Pan, H. Rao, X. Zhong, 1D choline-PbI₃ based heterostructure boosts efficiency and stability of CsPbI₃ perovskite solar cells, *Angew. Chem.* 135 (25) (2023), <https://doi.org/10.1002/ange.202303486>.
- [29] G. Zhang, J. Zhang, Z. Yang, Z. Pan, H. Rao, X. Zhong, Role of moisture and oxygen in defect management and orderly oxidation boosting carbon-based CsPbI₂Br solar cells to a new record efficiency, *Adv. Mater.* 34 (40) (2022), 2206222, <https://doi.org/10.1002/adma.202206222>.
- [30] Y. Liao, J. Zhang, W. Wang, Z. Yang, R. Huang, J. Lin, L. Che, G. Yang, Z. Pan, H. Rao, X. Zhong, Anti-dissociation passivation via bidentate anchoring for efficient carbon-based CsPbI_{2.6}Br_{0.4} solar cells, *Adv. Funct. Mater.* 33 (20) (2023), <https://doi.org/10.1002/adfm.202214784>.
- [31] Z. Ku, Y. Rong, M. Xu, T. Liu, H. Han, Full printable processed mesoscopic CH₃NH₃PbI₃/TiO₂ heterojunction solar cells with carbon counter electrode, *Sci. Rep.* 3 (1) (2013) 3132, <https://doi.org/10.1038/srep03132>.
- [32] H. Zhang, Y. Li, S. Tan, Z. Chen, K. Song, S. Huang, J. Shi, Y. Luo, D. Li, Q. Meng, High-efficiency (>20%) planar carbon-based perovskite solar cells through device configuration engineering, *J. Colloid Interface Sci.* 608 (2022) 3151–3158, <https://doi.org/10.1016/j.jcis.2021.11.050>.
- [33] H. Zhou, Y. Shi, K. Wang, Q. Dong, X. Bai, Y. Xing, Y. Du, T. Ma, Low-temperature processed and carbon-based ZnO/CH₃NH₃PbI₃/C planar heterojunction perovskite solar cells, *J. Phys. Chem. C* 119 (9) (2015) 4600–4605, <https://doi.org/10.1021/jp512101d>.
- [34] F. Deng, X. Sun, X. Lv, Y. Li, S. Li, Y.Z. Zheng, X. Tao, All room-temperature processing efficient planar carbon-based perovskite solar cells, *J. Power Sources* 489 (2021), 229345, <https://doi.org/10.1016/j.jpowsour.2020.229345>.
- [35] C. Peng, H. Su, J. Li, Q. Duan, Q. Li, J. Xiao, Z. Ku, J. Zhong, W. Li, Y. Peng, F. Huang, Y. Cheng, Scalable, efficient and flexible perovskite solar cells with carbon film based electrode, *Sol. Energy Mater. Sol. Cells* 230 (2021), 111226, <https://doi.org/10.1016/j.solmat.2021.111226>.
- [36] W. Passatorntaschakorn, C. Bhoomanee, P. Ruankham, A. Gardchareon, P. Songsiririthigul, D. Wongrataphisan, Room-temperature carbon electrodes with ethanol solvent interlacing process for efficient and stable planar hybrid perovskite solar cells, *Energy Rep.* 7 (2021), <https://doi.org/10.1016/j.egyr.2021.04.031>.
- [37] S. Abbasi, X. Wang, P. Tipparak, C. Bhoomanee, P. Ruankham, H. Liu, D. Wongrataphisan, W. Shen, Proper annealing process for a cost effective and superhydrophobic ambient-atmosphere fabricated perovskite solar cell, *Mater. Sci. Semicond. Process.* 155 (2023), 107241, <https://doi.org/10.1016/j.mssp.2022.107241>.
- [38] S. Abbasi, P. Ruankham, W. Passatorntaschakorn, W. Khampa, W. Musikpan, C. Bhoomanee, H. Liu, D. Wongrataphisan, W. Shen, A new single-step technique to fabricate transparent hydrophobic surfaces utilizable in perovskite solar cells, *Appl. Surf. Sci.* 613 (2023), 155969, <https://doi.org/10.1016/j.apsusc.2022.155969>.
- [39] W. Khampa, C. Bhoomanee, W. Musikpan, W. Passatorntaschakorn, C. Rodwiok, H.S. Kim, A. Gardchareon, P. Ruankham, D. Wongrataphisan, A passivation by H₂O₂/TiO₂ interlayer for efficient and stable carbon-based perovskite solar cells, *Appl. Surf. Sci.* 637 (2023), 157933, <https://doi.org/10.1016/j.apsusc.2023.157933>.
- [40] N. Khambunkoed, S. Homnan, A. Gardchareon, N. Chattrapiban, P. Songsiririthigul, D. Wongrataphisan, P. Ruankham, Fully-covered slot-die-coated ZnO thin films for reproducible carbon-based perovskite solar cells, *Mater. Sci. Semicond. Process.* 136 (2021), 106151, <https://doi.org/10.1016/j.mssp.2021.106151>.
- [41] N. Khambunkoed, D. Wongrataphisan, A. Gardchareon, N. Chattrapiban, S. Homnan, P. Songsiririthigul, P. Ruankham, Slot-die-coated zinc tin oxide film for carbon-based methylammonium-free perovskite solar cells, *Surf. Rev. Lett.* 28 (11) (2021), <https://doi.org/10.1142/S0218625X21501092>.
- [42] S. Homnan, P. Malison, K. Amratisha, P. Kanjanaboons, D. Wongrataphisan, T. Sagawa, P. Ruankham, Low-temperature processable Sn-doped ZnO films as electron transporting layers for perovskite solar cells, *J. Mater. Sci. Mater. Electron.* 32 (23) (2021) 27279–27289, <https://doi.org/10.1007/s10854-021-07097-6>.
- [43] P. Makming, S. Homnan, A. Ngamjaruojana, S. Rimjaem, A. Gardchareon, T. Sagawa, M. Haruta, P. Pakawatpanurut, D. Wongrataphisan, P. Kanjanaboons, A. Intaniwet, P. Ruankham, Efficient and stable carbon-based perovskite solar cells enabled by mixed CuPc:CuSCN hole transporting layer for indoor applications, *ACS Appl. Mater. Interfaces* 15 (12) (2023) 15486–15497, <https://doi.org/10.1021/acsmi.2c23136>.
- [44] P. Ruankham, N. Khambunkoed, P. Kanjanaboons, D. Wongrataphisan, T. Sagawa, Improved reproducibility of carbon-based cesium/formamidinium perovskite solar cells via double antisolvent drippings in adduct approach, *Org. Electron.* 100 (2022), 106362, <https://doi.org/10.1016/j.orgel.2021.106362>.
- [45] L. Gao, J. Hu, F. Meng, Y. Zhou, Y. Li, G. Wei, T. Ma, Comparison of interfacial bridging carbon materials for effective carbon-based perovskite solar cells, *J. Colloid Interface Sci.* 579 (2020) 425–430, <https://doi.org/10.1016/j.jcis.2020.06.090>.
- [46] H. Su, J. Xiao, Q. Li, C. Peng, X. Zhang, C. Mao, Q. Yao, Y. Lu, Z. Ku, J. Zhong, W. Li, Y. Peng, F. Huang, Y. Cheng, Carbon film electrode based square-centimeter scale planar perovskite solar cells exceeding 17% efficiency, *Mater. Sci. Semicond. Process.* 107 (2020), 104809, <https://doi.org/10.1016/j.mssp.2019.104809>.
- [47] D. Li, P. Jiang, W. Zhang, J. Du, C. Qiu, J. Liu, Y. Hu, Y. Rong, A. Mei, H. Han, Series resistance modulation for large-area fully printable mesoscopic perovskite solar cells, *Sol. RRL* 6 (3) (2022), 2100554, <https://doi.org/10.1002/solr.202100554>.
- [48] W. Thongsamrit, C. Phrompet, K. Maneesai, A. Karaphun, W. Tuichai, C. Sriwong, C. Ruttanapun, Effect of grain boundary interfaces on electrochemical and thermoelectric properties of a Bi₂Te₃/reduced graphene oxide composites, *Mater. Chem. Phys.* 250 (2020), 123196, <https://doi.org/10.1016/j.matchemphys.2020.123196>.
- [49] N. Khongchareon, S. Choopun, N. Hongsith, A. Gardchareon, S. Phadungdhitidhada, D. Wongrataphisan, Influence of carbon nanotubes in gel electrolyte on photovoltaic performance of ZnO dye-sensitized solar cells, *Electrochim. Acta* 106 (2013) 195–200, <https://doi.org/10.1016/j.electacta.2013.05.096>.
- [50] C. Rodwiok, T. Tam, W.M. Choi, M. Suwannakaew, S.W. Woo, D. Wongrataphisan, H.S. Kim, Preparation and characterization of photoluminescent graphene quantum dots from watermelon rind waste for the detection of ferric ions and cellular bio-imaging applications, *Nanomaterials* 12 (4) (2022) 702, <https://doi.org/10.3390/nano12040702>.

- [51] H. Tan, A. Jain, O. Voznyy, X. Lan, F.P. García de Arquer, J.Z. Fan, R. Quintero-Bermudez, M. Yuan, B. Zhang, Y. Zhao, F. Fan, P. Li, L.N. Quan, Y. Zhao, Z.H. Lu, Z. Yang, S. Hoogland, E.H. Sargent, Efficient and stable solution-processed planar perovskite solar cells via contact passivation, *Science* 355 (6326) (2017) 722–726, <https://doi.org/10.1126/science.aai9081>.
- [52] A. Prathan, J. Sanglao, T. Wang, C. Bhoomanee, P. Ruankham, A. Gardchareon, D. Wongratanaaphisan, Controlled structure and growth mechanism behind hydrothermal growth of TiO_2 nanorods, *Sci. Rep.* 10 (1) (2020) 8065, <https://doi.org/10.1038/s41598-020-64510-6>.
- [53] C. Bhoomanee, J. Sanglao, P. Kumnorkaew, T. Wang, K. Lohawet, P. Ruankham, A. Gardchareon, D. Wongratanaaphisan, Hydrothermally treated TiO_2 nanorods as electron transport layer in planar perovskite solar cells, *Phys. Status Solidi* 218 (1) (2021), 2000238, <https://doi.org/10.1002/pssa.202000238>.
- [54] F. Cai, L. Yang, Y. Yan, J. Zhang, F. Qin, D. Liu, Y.B. Cheng, Y. Zhou, T. Wang, Eliminated hysteresis and stabilized power output over 20% in planar heterojunction perovskite solar cells by compositional and surface modifications to the low-temperature-processed TiO_2 layer, *J. Mater. Chem. A* 5 (19) (2017) 9402–9411, <https://doi.org/10.1039/C7TA02317K>.
- [55] H. Zhang, J. Xiao, J. Shi, H. Su, Y. Luo, D. Li, H. Wu, Y.B. Cheng, Q. Meng, Self-adhesive macroporous carbon electrodes for efficient and stable perovskite solar cells, *Adv. Funct. Mater.* 28 (39) (2018), 1802985, <https://doi.org/10.1002/adfm.201802985>.
- [56] S. Jing, Y. Zhao, R.C. Sun, L. Zhong, X. Peng, Facile and high-yield synthesis of carbon quantum dots from biomass-derived carbons at mild condition, *ACS Sustain. Chem. Eng.* 7 (8) (2019) 7833–7843, <https://doi.org/10.1021/acssuschemeng.9b00027>.
- [57] A.B.D. Nandyanto, R. Oktiani, R. Ragadhitia, How to read and interpret FTIR spectroscopy of organic material, *Indones. J. Sci. Technol.* 4 (1) (2019) 97, <https://doi.org/10.17509/ijost.v4i1.15806>.
- [58] B. Pakhira, M. Ghosh, A. Allam, S. Sarkar, Carbon nano onions cross the blood brain barrier, *RSC Adv.* 6 (35) (2016) 29779–29782, <https://doi.org/10.1039/C5RA23534K>.
- [59] C. Rodwihok, D. Wongratanaaphisan, Y.L. Thi Ngo, M. Khandelwal, S.H. Hur, J. S Chung, Effect of GO additive in ZnO/rGO nanocomposites with enhanced photosensitivity and photocatalytic activity, *Nanomaterials* 9 (10) (2019) 1441, <https://doi.org/10.3390/nano9101441>.
- [60] C. Gu, H. Zhang, X. Wang, J. Tu, Synthesis of reduced graphene oxide by an ionothermal method and electrochemical performance, *RSC Adv.* 3 (29) (2013) 11807, <https://doi.org/10.1039/c3ra41485j>.
- [61] S.G. Kim, O.K. Park, J.H. Lee, B.C. Ku, Layer-by-layer assembled graphene oxide films and barrier properties of thermally reduced graphene oxide membranes, *Carbon Lett.* 14 (4) (2013) 247–250, <https://doi.org/10.5714/CL.2013.14.4.247>.
- [62] K.V. Sankar, R.K. Selvan, R.H. Vignesh, Y.S. Lee, Nitrogen-doped reduced graphene oxide and aniline based redox additive electrolyte for a flexible supercapacitor, *RSC Adv.* 6 (72) (2016) 67898–67909, <https://doi.org/10.1039/C6RA11521G>.
- [63] K.V. Sankar, R.K. Selvan, The preparation of MnFe₂O₄ decorated flexible graphene wrapped with PANI and its electrochemical performances for hybrid supercapacitors, *RSC Adv.* 4 (34) (2014) 17555, <https://doi.org/10.1039/c3ra47681b>.
- [64] D.J. Kim, J.M. Yoo, Y. Suh, D. Kim, I. Kang, J. Moon, M. Park, J. Kim, K.S. Kang, B. Hong, Graphene quantum dots from carbonized coffee bean wastes for biomedical applications, *Nanomaterials* 11 (6) (2021) 1423, <https://doi.org/10.3390/nano11061423>.
- [65] K. Huang, H. Yu, M. Xie, S. Liu, F. Wu, Effects of poly(ethylene glycol)-grafted graphene on the electrical properties of poly(lactic acid) nanocomposites, *RSC Adv.* 9 (19) (2019) 10599–10605, <https://doi.org/10.1039/C9RA01060B>.
- [66] L. Wang, W.M. Choi, J.S. Chung, S.H. Hur, Multicolor emitting N-doped carbon dots derived from ascorbic acid and phenylenediamine precursors, *Nanoscale Res. Lett.* 15 (1) (2020) 222, <https://doi.org/10.1186/s11671-020-03453-3>.
- [67] D.K. Dang, C. Sundaram, Y.L.T. Ngo, J.S. Chung, E.J. Kim, S.H. Hur, One pot solid-state synthesis of highly fluorescent N and S co-doped carbon dots and its use as fluorescent probe for Ag⁺ detection in aqueous solution, *Sens. Actuators B* 255 (2018) 3284–3291, <https://doi.org/10.1016/j.snb.2017.09.155>.
- [68] Y. Chen, S. Wu, X. Li, M. Liu, Z. Chen, P. Zhang, S. Li, Efficient and stable low-cost perovskite solar cells enabled by using surface passivated carbon as the counter electrode, *J. Mater. Chem. C* 10 (4) (2022) 1270–1275, <https://doi.org/10.1039/D1TC05351E>.
- [69] Y. Zhao, J. Wei, H. Li, Y. Yan, W. Zhou, D. Yu, Q. Zhao, A polymer scaffold for self-healing perovskite solar cells, *Nat. Commun.* 7 (1) (2016) 10228, <https://doi.org/10.1038/ncomms10228>.
- [70] H. Xie, X. Yin, Y. Guo, D. Liu, T. Liang, G. Wang, W. Que, Hole transport free flexible perovskite solar cells with cost-effective carbon electrodes, *Nanotechnology* 32 (10) (2021), 105205, <https://doi.org/10.1088/1361-6528/abc70>.
- [71] H. Wei, J. Xiao, Y. Yang, S. Lv, J. Shi, X. Xu, J. Dong, Y. Luo, D. Li, Q. Meng, Free-standing flexible carbon electrode for highly efficient hole-conductor-free perovskite solar cells, *Carbon* 93 (2015) 861–868, <https://doi.org/10.1016/j.carbon.2015.05.042>.
- [72] T. Smerchit, N. Thongprong, W. Ruengsrisang, I.M. Adam, K.T. Soe, S. Thansamai, N. Chanlek, H. Nakajima, R. Supruangnet, V. Saetang, A. Kaewprajak, T. Supasai, N. Rujisamphan, Combined experimental and simulation studies of lithium and cobalt-modified TiO_2 and their impacts on the performance and stability of perovskite solar cells, *Adv. Mater. Interfaces* 9 (31) (2022), 2201632, <https://doi.org/10.1002/admi.202201632>.
- [73] C. Bonavolontà, A. Vettoliere, G. Falco, C. Aramo, I. Rendina, B. Ruggiero, P. Silvestrini, M. Valentino, Reduced graphene oxide on silicon-based structure as novel broadband photodetector, *Sci. Rep.* 11 (1) (2021) 13015, <https://doi.org/10.1038/s41598-021-92518-z>.
- [74] R. Wang, J. Xue, L. Meng, J.W. Lee, Z. Zhao, P. Sun, L. Cai, T. Huang, Z. Wang, Z. K. Wang, Y. Duan, J.L. Yang, S. Tan, Y. Yuan, Y. Huang, Y. Yang, Caffeine improves the performance and thermal stability of perovskite solar cells, *Joule* 3 (6) (2019) 1464–1477, <https://doi.org/10.1016/j.joule.2019.04.005>.
- [75] M. Elawad, K.I. John, A.M. Idris, L. Yang, Y. Gao, An organic hole-transporting material spiro-OMeTAD doped with a Mn complex for efficient perovskite solar cells with high conversion efficiency, *RSC Adv.* 11 (52) (2021) 32730–32739, <https://doi.org/10.1039/D1RA05906H>.
- [76] Z. Li, J. Chen, H. Li, Q. Zhang, Z. Chen, X. Zheng, G. Fang, H. Wang, Y. Hao, A facilely synthesized ‘spiro’ hole-transporting material based on spiro[3.3]heptane-2,6-dispirofluorene for efficient planar perovskite solar cells, *RSC Adv.* 7 (66) (2017) 41903–41908, <https://doi.org/10.1039/C7RA06643K>.
- [77] Z. Wu, Z. Liu, Z. Hu, Z. Hawash, L. Qiu, Y. Jiang, L.K. Ono, Y. Qi, Highly efficient and stable perovskite solar cells via modification of energy levels at the perovskite/ carbon electrode interface, *Adv. Mater.* 31 (11) (2019), 1804284, <https://doi.org/10.1002/adma.201804284>.
- [78] K. Yan, Z. Wei, J. Li, H. Chen, Y. Yi, X. Zheng, X. Long, Z. Wang, J. Wang, J. Xu, S. Yang, High-performance graphene-based hole conductor-free perovskite solar cells: Schottky junction enhanced hole extraction and electron blocking, *Small* 11 (19) (2015) 2269–2274, <https://doi.org/10.1002/smll.201403348>.
- [79] Y. Wang, W.Y. Rho, H.Y. Yang, T. Mahmodi, S. Seo, D.H. Lee, Y.B. Hahn, Air-stable, hole-conductor-free high photocurrent perovskite solar cells with $CH_3NH_3PbI_3$ -NiO nanoparticles composite, *Nano Energy* 27 (2016) 535–544, <https://doi.org/10.1016/j.nanoen.2016.08.006>.
- [80] P. Schulz, A.M. Dowgiallo, M. Yang, K. Zhu, J.L. Blackburn, J.J. Berry, Charge transfer dynamics between carbon nanotubes and hybrid organic metal halide perovskite films, *J. Phys. Chem. Lett.* 7 (3) (2016) 418–425, <https://doi.org/10.1021/acs.jpclett.5b02721>.
- [81] J. Ghosh, R. Ghosh, P.K. Giri, Mesoporous Si Nanowire Templated Controlled Fabrication of Organometal Halide Perovskite Nanoparticles with High Photoluminescence Quantum Yield for Light-Emitting Applications, *ACS Applied Nano Materials* 1 (4) (2018) 1551–1562, <https://doi.org/10.1021/acsnano.8b00047>.
- [82] H. Chen, T. Liu, P. Zhou, S. Li, J. Ren, H. He, J. Wang, N. Wang, S. Guo, Efficient bifacial passivation with crosslinked thioctic acid for high-performance methylammonium lead iodide perovskite solar cells, *Adv. Mater.* 32 (6) (2020), 1905661, <https://doi.org/10.1002/adma.201905661>.
- [83] Q. Lou, H. Li, Q. Huang, Z. Shen, F. Li, Q. Du, M. Jin, C. Chen, Multifunctional CNT: TiO_2 additives in spiro-OMeTAD layer for highly efficient and stable perovskite solar cells, *EcoMat* 3 (3) (2021), <https://doi.org/10.1002/eom2.12099>.
- [84] R. Ihly, A.M. Dowgiallo, M. Yang, P. Schulz, N.J. Stanton, O.G. Reid, A.J. Ferguson, K. Zhu, J.J. Berry, J.L. Blackburn, Efficient charge extraction and slow recombination in organic-inorganic perovskites capped with semiconducting single-walled carbon nanotubes, *Energy Environ. Sci.* 9 (4) (2016) 1439–1449, <https://doi.org/10.1039/C5EE03806E>.
- [85] J. Shi, D. Li, Y. Luo, H. Wu, Q. Meng, Opto-electro-modulated transient photovoltage and photocurrent system for investigation of charge transport and recombination in solar cells, *Rev. Sci. Instrum.* 87 (12) (2016), 123107, <https://doi.org/10.1063/1.4972104>.
- [86] M.V. Khenkin, E.A. Katz, A. Abate, G. Bardizza, J.J. Berry, C. Brabec, F. Brunetti, V. Bulović, Q. Burlingame, A. di Carlo, R. Cheacharoen, Y.B. Cheng, A. Colsmann, S. Cros, K. Domanski, M. Dusza, C.J. Fell, S.R. Forrest, Y. Galagan, M. Lira-Cantu, Consensus statement for stability assessment and reporting for perovskite photovoltaics based on ISOS procedures, *Nature Energy* 5 (1) (2020) 35–49, <https://doi.org/10.1038/s41560-019-0529-5>.